Available online at www.sciencedirect.com
ScienceDirect
International Journal of Multiphase Flow 32 (2006) 1191–1218
International Journal of Multiphase Flow
www.elsevier.com/locate/ijmulflow

Experimental study on hydrodynamic characteristics of upward gas–liquid slug flow

Donghong Zheng, Defu Che *

State Key Laboratory of Multiphase Flow in Power Engineering, Xi'an Jiaotong University, Xi'an 710049, China

Received 30 November 2005; received in revised form 17 May 2006

Abstract

To clarify the impacts of the hydrodynamic boundary layer and the diffusion boundary layer in the near wall zone on gas–liquid two-phase flow induced corrosion in pipelines, the hydrodynamic characteristics of fully developed gas–liquid slug flow in an upward tube are investigated with limiting diffusion current probes, conductivity probes and digital high-speed video system. The Taylor bubble and the falling liquid film characteristics are studied, the effects of various factors are examined, and the experimental results are compared with the data and models available in literature. The length of Taylor bubble, the local void fraction of the slug unit and the liquid slug, the shear stress and mass transfer coefficient in the near wall zone, are all increased with the increase of superficial gas velocity and decreased with the increase of superficial liquid velocity, whereas the length of liquid slug and the liquid slug frequency are changed contrarily. The alternate wall shear stress due to upward gas–liquid slug flow is considered to be one of the major causes for the corrosion production film fatigue cracking. A normalized formula for mass transfer coefficient is obtained based on the experimental data.
© 2006 Elsevier Ltd. All rights reserved.

Keywords: Gas–liquid slug flow; Taylor bubble; Falling liquid film; Wall shear stress; Mass transfer coefficient; Flow induced corrosion

1. Introduction

Gas–liquid slug flow is one of common flow regimes in gas and oil pipelines with a wide range of gas and oil transport rates. Recently, scientists and engineers have paid more attention to the internal corrosion of low alloy pipelines, in which the gas–liquid mixtures of CO_2, H_2S, oil, and water are transported. CO_2 or H_2S dissolves in the water to form the weak acid, which makes low alloy pipelines suffer from serious corrosion. This corrosion is referred to as upward gas–liquid slug flow induced "CO_2 sweet corrosion" or "H_2S sour corrosion" (Garber, 1998; Nesic and Lunde, 1994; Heuer and Stubbins, 1998; Jasinski, 1987; Heitz, 1991). How to effectively control the upward gas–liquid slug flow induced corrosion in the pipelines is challenging scientists and engineers all over the world.

---

* Corresponding author. Tel.: +86 29 82665185; fax: +86 29 82668703.
E-mail address: dfche@mail.xjtu.edu.cn (D. Che).

0301-9322/$ - see front matter © 2006 Elsevier Ltd. All rights reserved.
doi:10.1016/j.ijmultiphaseflow.2006.05.012

Previous research on the CO_2 or H_2S corrosion has been done mostly in stirred beaker, rotating cylinder electrode cell, jet impingement and single phase flow loop on a small scale. The effect of gas–liquid flow on the corrosion has been seldom considered and the experimental conditions are considerably different from practical industrial corrosion conditions (Heuer and Stubbins, 1998; Liu et al., 1994; Lotz and Syberger, 1988; Nesic et al., 1995; Hara et al., 2000). As known to all, corrosion is a surface damage phenomenon. Therefore, what is going on at the metal surface has a profound effect on corrosion (Mora-Mendoza et al., 2002; Heitz, 1991). Many aspects of fluid dynamics related to or determined by the interactions between fluid and metal surface are of importance to corrosion. The changes in fluid hydrodynamics, turbulence, wall shear stress, mass transfer, electrochemical corrosion, the formation and the destruction of the corrosion production film, are all intimately related to the hydrodynamic boundary layer and the diffusion boundary layer in the vicinity of the wall.

Therefore, there is an urgent need for the deep insight into the upward slug flow characteristics to understand the mechanism of gas–liquid slug flow induced corrosion. The remarkable characteristic of the slug flow is the flow intermittence, which is influenced by many factors, such as the velocities of gas and liquid, void fraction, pressure shock, density wave, liquid slug frequency and the properties of gas and liquid (Fernandes et al., 1983). In the upward slug flow, the complicated slug flow structure can be described as a series of slug units, and each unit consists of a Taylor bubble with a falling liquid film around it and a portion of liquid slug behind the Taylor bubble. Under the gravitational force, the falling liquid film is assimilated by the succeeding liquid slug (Griffith and Wallis, 1961; Bendiksen, 1985; Taitel et al., 1980; Sylvester, 1987; Hewitt, 1990; Mao and Dukler, 1985; Nakoryakov et al., 1986; van Hout et al., 2001; Ghosh and Cui, 1999).

In this paper, using the limiting diffusion current technology, conductivity probe technology and digital high-speed video system, the characteristics of upward slug flow are systematically investigated both experimentally and mechanistically. These characteristics include the Taylor bubble velocity, the Taylor bubble nose shape, the thickness and velocity of falling film, minimum stable liquid slug length, the bubble size distribution and the velocity of dispersion bubble in liquid slug, the liquid slug frequency, the length distribution of Taylor bubble and liquid slug, the void fraction of slug unit and liquid slug, instantaneous shear stress and mass transfer coefficient in the near wall zone.

2. Experimental

2.1. Experimental set-up

The experiments are conducted in a two-phase flow loop, the schematic diagram of which is shown in Fig. 1. The gas stored in gas storage vessel 1 is pressurized for recirculation by twin-screw compressor 11,

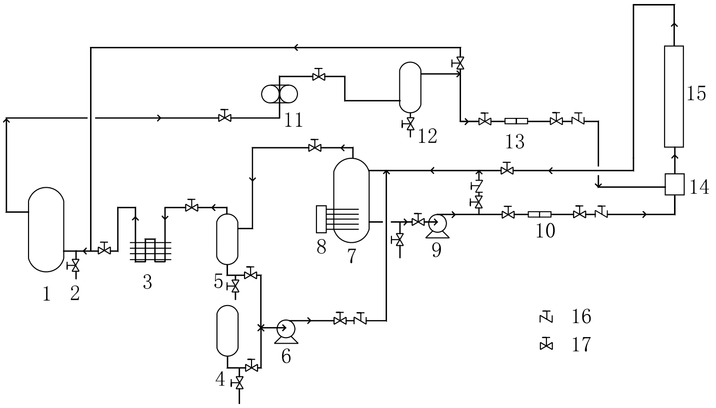

Fig. 1. Schematic diagram of experimental set-up: (1) gas storage vessel; (2) gas supplement device; (3) freezing dryer; (4) liquid supplement tank; (5) secondary separator; (6) secondary pump; (7) liquid storage tank; (8) oil bath heater; (9) primary pump; (10) liquid phase orifice flowmeter; (11) twin-screw compressor; (12) gas surge tank; (13) gas phase orifice flowmeter; (14) two-phase mixing device; (15) test section; (16) non-return valve; (17) cut off valve.

whereas the liquid stored in liquid storage tank 7 is driven by primary pump 9 for recirculation. The flows of both gas and liquid are regulated respectively by the combination of valves and by-passages before they are measured by gas phase orifice flowmeter 13 and liquid phase orifice flowmeter 10. The gas phase and the liquid phase are mixed in mixing device 14 before they enter test section 15. When the two-phase mixture flows out of the test section, the liquid phase and the gas phase are primarily separated in liquid storage tank 7 and secondarily separated in secondary separator 5. The separated gas is dried by freezing dryer 3 for the elimination of moisture before the gas reenters compressor 11, whereas the separated liquid in secondary separator 5 is driven to liquid storage tank 7 by secondary pump 6. In the loop, by gas supplement device 2 and liquid supplement tank 4, gas and liquid can be supplemented to the experimental system whenever necessary, and oil bath heater 8 is installed on liquid storage tank 7 to control the temperature of the fluids to be studied. Additionally, 12 is a gas surge tank, whereas 16 and 17 are the non-return valve and cut-off valve, respectively.

The test section is a vertical 35 mm inside diameter, 5 m long Plexiglas pipe, schematically shown in Fig. 2. The pressure differential with a distance of 1570 mm is measured by the 1151DP type capacitance differential pressure transmitter made in China with an accuracy of 0.3%. To obtain stable differential pressure, the connecting pipes are firstly connected to two little surge tanks before they are connected to the transmitter, and a manometer is installed downstream of the connecting pipe to measure the local absolute pressure. Wall mass transfer probe and wall shear stress probe are used to measure the mass transfer coefficient and the shear stress

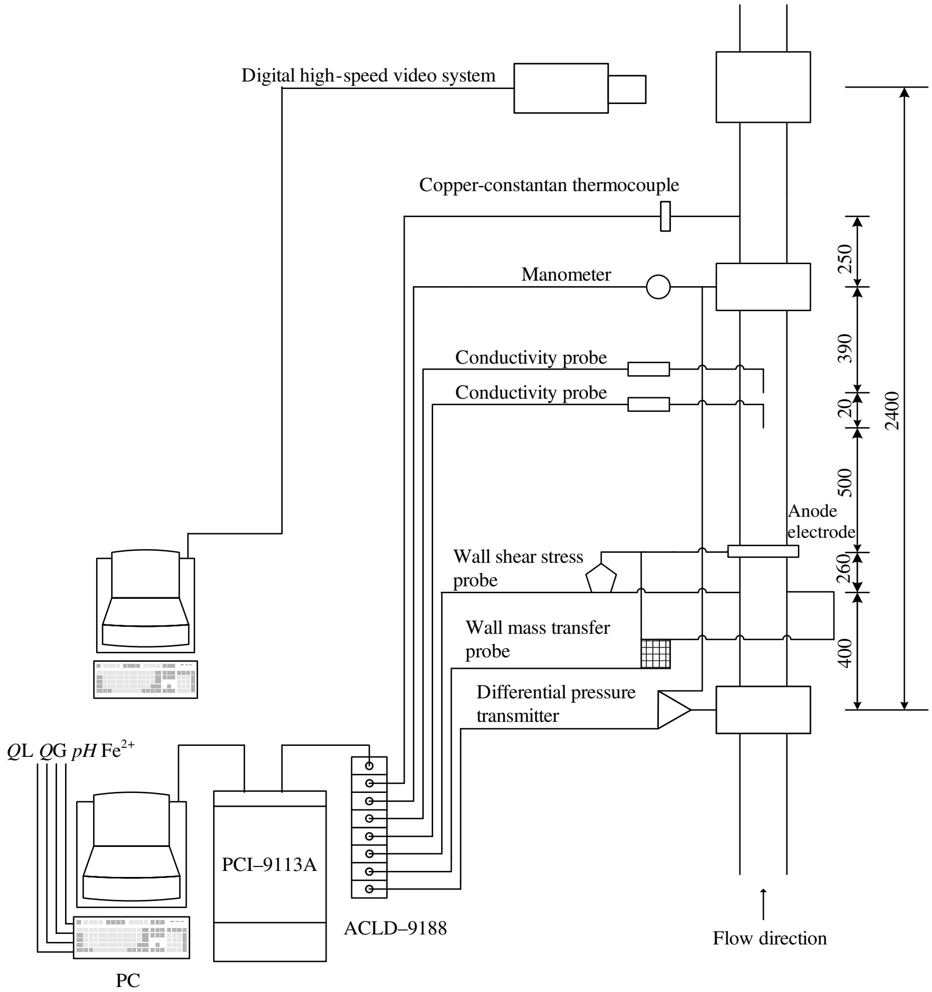

Fig. 2. Schematic diagram of test section.

in the near wall zone and the measurement principle is elucidated in Section 2.2. Two conductivity probes are the same single sensor conductivity probe and the measurement principle is illustrated in Section 2.3. A copper–constantan thermocouple with the maximum temperature deviation of 0.2 °C is installed to measure the experimental temperature. A digital high-speed video system is installed at the downstream of test section and the measurement principle is explained in Section 2.4.

2.2. Electrochemical limiting diffusion current technology

The electrochemical limiting diffusion current technology called polarography was used by Hanratty and Reiss (1962), Reiss and Hanratty (1963), Gognet and Lebouche (1978), Souhar and Cognet (1978) and Nakoryakov and Kashinsky (1981), Nakoryakov et al. (1986) to investigate the characteristics of gas–liquid two-phase flow. When a proper voltage is applied across the electrodes which are dipped into the electrolyte, the electrolysis current I, which results from active ions transfer to the electrodes, is controlled by both concentration gradient due to diffusion $D_d(\partial C/\partial x)$ and electric potential gradient due to migration $C_u(\partial\psi/\partial x)$, namely

$$\frac{I}{nAF} = -\left(D_d\frac{\partial C}{\partial x} + C_u\frac{\partial\psi}{\partial x}\right) \tag{1}$$

where n is number of electrons involved in the stoichiometric equation, A area, F Faraday constant, D_d diffusion coefficient, C_u electric potential migration coefficient, C concentration and ψ electric potential.

With the increase of applied voltage, the rate of the reaction occurring on the electrodes is increased and the reaction ion concentration on the electrodes C_w is decreased. When the electrolyte with high conductance and inert to the electrode reaction is added into the solution, the electric potential gradient $C_u(\partial\psi/\partial x)$ approaches zero and can be ignored. If the reaction ion concentration on the electrodes C_w approaches zero, the reaction rate on the electrodes becomes maximum. Meanwhile, the electrolysis current I is completely controlled by the concentration diffusion gradient, and the current I is no more changed with the increase of applied voltage, namely a voltage plateau appears. Then, this condition is called polarization and the current I is called limiting diffusion current $I_{\lim}$. According to Nernst's linear concentration gradient assumption, we have

$$\frac{I_{\lim}}{nAF} = \frac{D_d}{\delta}(C_b - C_w)|_{C_w=0} = \frac{D_d}{\delta}C_b = k_d C_b \tag{2}$$

$$k_d = \frac{I_{\lim}}{nAFC_b} \tag{3}$$

where δ is concentration boundary thickness, C_b concentration in bulk solution zone, and k_d mass transfer coefficient.

Therefore, using the limiting diffusion current $I_{\lim}$, the mass transfer coefficient k_d in the near wall zone can be obtained. Hanratty and Reiss (1962) and Reiss and Hanratty (1963) found that the relationship between the mass transfer coefficient and wall shear stress can be represented by

$$k_d = 0.807D_d\left(\frac{\tau_w}{\mu_L D_d L}\right)^{1/3} \tag{4}$$

where τ_w is wall shear stress, μ_L liquid dynamic viscosity and L electrode width in the flow direction.

Thus, the wall shear stress τ_w in the near wall zone can also be obtained. From the above analyses, it can easily be found that the mass transfer coefficient k_d is proportional to the limiting diffusion current, whereas the wall shear stress is cubic power to the limiting diffusion current.

In the experiments, the electrolyte of 0.5 mol/L NaOH–0.01 mol/L $K_4Fe(CN)_6$–0.01 mol/L $K_3Fe(CN)_6$ is produced as the experimental liquid, and N_2 is used as the experimental gas.

Wall mass transfer probe, which is a small rectangular 1 mm × 0.06 mm pure Ni slice film and mounted flush to the wall across the flow direction, is used to measure the mass transfer coefficient. Wall shear stress probe, which is made up of double pure Ni slice films with the same geometric dimensions as wall mass transfer probe and an insulating mica film with a thickness of 0.1 mm is sandwiched between the double pure Ni slice films, is used to measure the magnitude and direction of wall shear stress.

Wall shear stress probe can easily detect the magnitude and direction of the shear stress in the near wall zone. As shown in Fig. 3, due to the small distance between the double slice films, the loss of reaction ions on the upstream film of the probe is unable to be recovered sufficiently when the fluid has reached the downstream of the probe, namely, when the fluid flows from film 1 to film 2, the concentration boundary layer thickness of film 1 is smaller than that of film 2, which correspondingly causes the diffusion rate or the limiting diffusion current of film 1 to be larger than that of film 2, $I_{\lim,1} > I_{\lim,2}$. On the other hand, when the fluid flows from film 2 to film 1, the concentration boundary layer thickness, the diffusion rate and the limiting diffusion current are all of the very reverse, $I_{\lim,1} < I_{\lim,2}$. From the above analyses, by comparing the limiting diffusion currents of both film 1 and film 2, the direction of the shear stress can be gained. A series of preparatory measurements must be performed before the two-phase flow measurements using the wall shear stress probe. The feedback resistances of two pieces of the direct current amplifiers must be repeatedly adjusted to eliminate any possible error caused by some inevitable difference in geometrical dimensions of the films so that identical output voltages of film 1 and 2 can be gained in the stagnant solution.

To improve the response of wall mass transfer probe and wall shear stress probe, a large anode ring, with a 1.5 mm thickness, 10 mm height, is mounted flush to the wall with a distance of 260 mm downstream of wall shear stress probe. In such a case, the effect of anode electrode on the limiting diffusion current can be ignored and the applied voltage between the cathode and the anode can be taken as the plateau voltage corresponding to the limiting diffusion current. The limiting diffusion current is so small that it must be transformed into the magnified voltage. Before the two-phase flow experiments, the plateau voltage is calibrated in the single liquid phase flow, using linear sweeping electric potential technology with the electrochemical workstation LK 2005 made in China. It is found that the plateau voltage appears when the applied voltage ranges from 0.25 V to 0.8 V, and then the applied voltage is taken as 0.5 V in the two-phase flow experiment.

2.3. Conductivity probe measurement technology

The principle of conductivity probe is the voltage drop caused by the electrical conductivity difference between gas phase and liquid phase, and has been widely used to measure the average fluctuating velocity, flow regime identification, film thickness, local and average void fraction, local bubble size, slug length

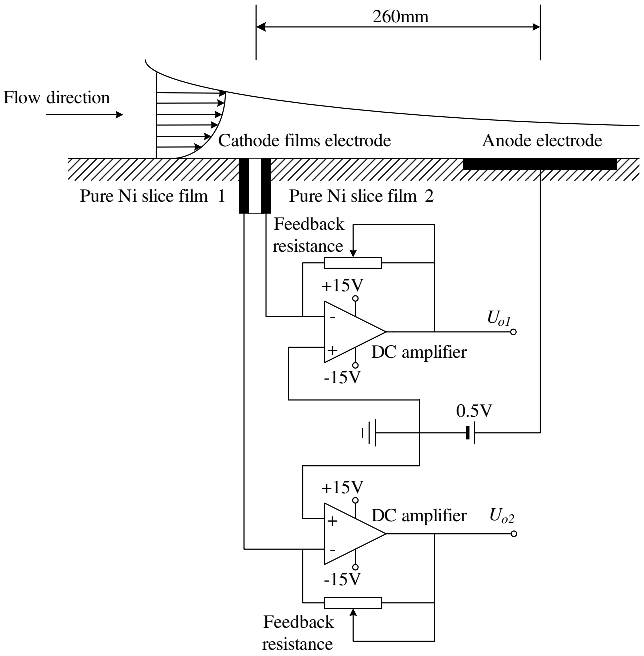

Fig. 3. Schematic diagram of the double electrochemical films probe for measuring the shear stress.

distribution, slug frequency, the coalescence and disintegration characteristic of bubbles etc. Over the last several decades, quite a few types of conductivity probes have been developed, such as level probe firstly designed and built by Kordyban and Ranov (1963), needle probe firstly designed by Solomon (1962) and further developed by Griffith (1963), wall probe developed by Collier and Hewitt (1964) and Hewitt and Lovegrove (1963).

Two conductivity needle probes have the same structure, both are made of nichrome alloy thread with 0.2 mm diameter, completely insulated and 90° bent, giving a 10 mm long tip. To make the probe able to quickly pierce through the bubble, and to have the smallest error induced by the bubble deformation when the bubble is in contact with the probe, the probe tip is corroded to a diameter of 50 μm by electrochemical method. Moreover, the length of non-insulated tip δ has an evident effect on the validity of acquired signal. If the length is too short, the interference coming from the flow field is not easily eliminated and the threshold voltage $U_{\text{threshold}}$ is difficult to be determined. On the other hand, if the length is too long, the time for the probe tip to be in contact with the gas phase or liquid phase will be too long, which also induces the poor validity of acquired signal. By a large number of tests, it is found that the optimal length of non-insulated tip is between 20 μm and 50 μm. Therefore, 35 μm non-insulated tip is used throughout the experiments. To gain the local and average information at different radial locations at certain cross section of the test section, a modified vernier calipers assembly with an accuracy of 0.02 mm is used to adjust and determine the location of the conductivity probe. Using the digital high-speed video system, the threshold voltage $U_{\text{threshold}}$ of conductivity probe is calibrated as 20% of the maximum output voltage. Therefore, a square wave function $P(t)$ exists

$$P(t) = \begin{cases} 0 & U < U_{\text{threshold}} \text{ when the probe in the liquid phase} \\ 1 & U > U_{\text{threshold}} \text{ when the probe in the gas phase} \end{cases} \tag{5}$$

The local average void fraction in time interval Δt is

$$\langle \alpha(\Delta t) \rangle = \frac{1}{n} \int_0^{\Delta t} P_i(\tau) = \frac{1}{n} \sum P_i(\tau), \quad \Delta t = n \cdot \tau \tag{6}$$

The flow velocity and the length of both Taylor bubble and liquid slug can be measured using two conductivity probes when they are located at the pipe axis with a distance ΔL and the signal voltage can be acquired simultaneously, as shown in Fig. 4. According to Δt_1, the Taylor bubble velocity U_{TB} is

$$U_{\text{TB}} = \frac{\Delta L}{\Delta t_1} \tag{7}$$

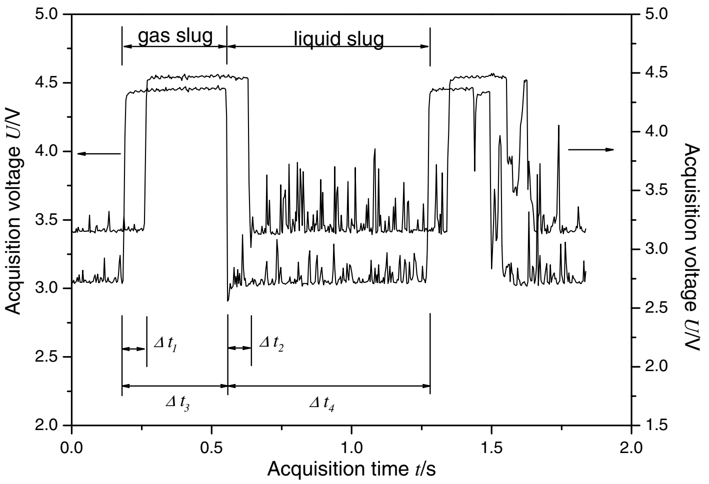

Fig. 4. Calculation method for the velocity and length of Taylor bubble and liquid slug in upward slug flow.

According to Δt_3, the Taylor bubble length L_{TB} is

$$L_{\mathrm{TB}} = U_{\mathrm{TB}} \Delta t_3 \tag{8}$$

Similarly, the succeeding liquid slug velocity U_{LS} can be obtained according to Δt_2, and the liquid length L_{LS} can be obtained according to Δt_4.

2.4. Digital high-speed video technology

The digital high-speed video system is based on the direct measurement principle of two-phase flow by shooting the photographs of the flow in a transparent Plexiglas pipe at a high speed. In the experiments, a MEMRECAM fx K3 digital high-speed video system, which is made up of camera, lens, trigger connector, AC supply, remote control panel, light source, transmission cable etc., is used to measure the flow characteristics. An advanced CMOS sensor device is installed in this system. The MEMRECAM fx K3 digital high-speed video system has a standard shooting speed of 2000 frames per second with 1.3 G memory size and 1280 × 1024 pixels. Due to the complicated gas–liquid interfaces, the light will suffer many times of refractions and reflections, which may lead to blurred pictures of the gas–liquid interfaces. Consequently, a cubic water pool made of quartz glass is installed on the test pipe to eliminate the refraction and reflection. A 1 kW diffusion cold light source is applied to make the light free from reflection on the lens surface. And back lighting is also applied to gain as clear gas–liquid interfaces as possible.

In processing the photographs, a scale factor is determined according to the outside diameter ($D = 45$ mm) of the test pipe. The scale factor F_{scale} is defined as

$$F_{\mathrm{scale}} = \frac{\text{pipe outside diameter in the photograph}}{\text{practical pipe outside diameter}} \tag{9}$$

F_{scale} is a very important parameter to obtain the real information from the photograph processing. The measurements of small bubble diameter, thickness of falling film and bubble nose size etc. can be easily performed in one photograph. Whereas, displacement and velocity of bubble can be measured in a series of succeeding photographs

$$U_i = \frac{1}{F_{\mathrm{scale}}} \frac{\sqrt{(\Delta x_i)^2 + (\Delta y_i)^2}}{\Delta \mathrm{frames} \cdot \tau} \tag{10}$$

where τ is the time interval between two continuous frames, Δx_i and Δy_i are the displacements measured in terms of the photographs.

2.5. Data acquisition system

A high-speed data acquisition card PCI-9113A made in Taiwan is used to acquire the experimental data. Acquisition signals are input with the differential 12-bit analog input and the sampling rate is 2 kHz per channel. The acquisition program is developed, based on the VC++, with real-time display, controllable sampling time and frequency.

Table 1
Experimental matrix in upward gas–liquid slug flow

Item	Scope
Superficial gas velocity (m/s)	0.1–0.8
Superficial liquid velocity (m/s)	0.2–1.2
Liquid phase	0.5 mol/L NaOH–0.01 mol/L $K_3Fe(CN)_6$–0.01 mol/L $K_4Fe(CN)_6$ $\rho_L = 1040$ kg/m^3, $\mu_L = 0.964 \times 10^{-3}$ Pa s, $\sigma_L = 0.010$ N/m Diffusion coefficient of $K_3Fe(CN)_6 D_d$ calculated as [a](Fouad and IbI, 1960)
Gas phase	N_2, the properties of N_2 calculated according to perfect gas law
Temperature (°C)	40
Pressure (MPa)	0.2
Single liquid phase flow velocity (m/s)	0.2–3.4

[a] $\frac{D_d \mu_L}{T} = 2.5 \times 10^{-15}$ N/K.

2.6. Experimental test matrix

The experimental matrix for upward gas–liquid slug flow is listed in Table 1.

3. Results and discussion

3.1. Flow characteristics in Taylor bubble zone

3.1.1. Gas Taylor bubble

Taylor bubble velocity is a very important parameter in upward gas–liquid slug flow. Dumitrescu (1943) was the first scientist to study single Taylor bubble rising in a stagnant liquid in a tube and he proposed a model for this flow, based on potential flow theory. Many other researchers including Moissis and Griffith (1962), Nicklin and Wilkes (1962), Street and Tek (1965), Akagawa and Sakaguchi (1966), also had further investigation of slug flow in stagnant liquids. Previous research shows that in a rather wide range of surface tension and viscosity, the Taylor bubble velocity is affected by many parameters such as gravity acceleration g, inside tube diameter D, superficial velocities of both gas and liquid, physical properties of fluids etc. A widely accepted formula for single, non-expanding Taylor bubble rising velocity in a stagnant liquid U_0 has been put forward as follows:

$$U_0 = C_2(N_\mathrm{f}, Eo)\sqrt{\frac{gD(\rho_\mathrm{L}-\rho_\mathrm{G})}{\rho_\mathrm{L}}} \tag{11}$$

where $N_\mathrm{f} = D^{3/2}\left(\frac{g(\rho_\mathrm{L}-\rho_\mathrm{G})}{\rho_\mathrm{L}}\right)^{1/2}\rho_\mathrm{L}/\mu_\mathrm{L}$, $Eo = \rho_\mathrm{L}\left(\frac{g(\rho_\mathrm{L}-\rho_\mathrm{G})}{\rho_\mathrm{L}}\right)D^2/\sigma$, and ρ_L is the liquid phase density, ρ_G the gas phase density, σ the surface tension.

In practical flows, $\rho_\mathrm{G} \ll \rho_\mathrm{L}$. A simplified formula is given as follows:

$$Fr_0 = \frac{U_0}{\sqrt{gD}} = C_2(N_\mathrm{f}, Eo) \tag{12}$$

C_2 has been derived theoretically, ranging from 0.32 to 0.36. $C_2 = 0.351$ by theory and $C_2 = 0.346$ by experiments were determined by Dumitrescu (1943), and $C_2 = 0.328$ was determined by Davies and Taylor (1950), whereas $C_2 = 0.35$ is consistent with both the experimental data in an air–water system of Nicklin (Nicklin and Wilkes, 1962) and the experimental data of Fernandes (1981).

In a fully developed upward slug flow, the Taylor bubble velocity can be regarded as steady, and the succeeding Taylor bubble is not affected by the leading Taylor bubble. As such, the fully developed upward slug flow can also be regarded as the rising flow of a single Taylor bubble in a flowing liquid. The rise velocity due to the buoyancy of Taylor bubble approaches the velocity of Taylor bubble rising in a stagnant liquid. As a result, the velocity of Taylor bubble in flowing liquid depends to a great extent on the mixture velocity and the rising velocity in stagnant liquid. Nicklin and Wilkes (1962), by a great number of experiments, suggested an empirical correlation for the rising velocity of the Taylor bubble U_TB in a flowing liquid as follows:

$$Fr_\mathrm{TB} = C_1 Fr_\mathrm{s} + C_2 \tag{13}$$

$$U_\mathrm{TB} = C_1 U_\mathrm{s} + U_0 \tag{14}$$

U_0 is the rising velocity in stagnant liquid, U_s is the mixture velocity defined as the sum of the liquid and gas superficial velocities, U_SL and U_SG. Collins and de Moraes (1978) provided a strong theoretical support for the Nicklin's formula. For fully developed turbulent flows ($Re_\mathrm{s} > 3000$), $C_1 = 1.2$, which is close to the ratio of the maximum centerline velocity U_c to the averaged mixture velocity U_s, namely $U_\mathrm{c}/U_\mathrm{s} = 1.225$, when the one seventh power velocity profile is assumed; for fully developed laminar flows ($Re_\mathrm{s} < 3000$), $C_1 = 2$, which is equal to the ratio $U_\mathrm{c}/U_\mathrm{s} = 2$ when the parabolic profile for the velocity is assumed. Fernandes (1981) suggested $C_1 = 1.29$, which is greater compared to the suggestion of Nicklin because of larger pipe diameter, expansion effects and interaction between successive Taylor bubbles. Schmidt (1976) and Juprasert (1976) investigated the air–water system with the same diameter pipe as Fernandes (1981) and suggested $C_1 = 1.2$.

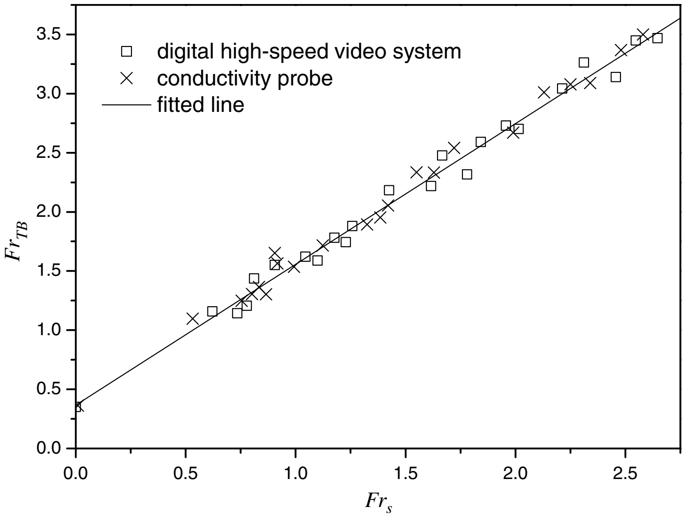

Fig. 5. Relationship between the Fr_s number based on mixture velocity and the Fr_{TB} number based on Taylor bubble velocity.

Fig. 5 shows the relationship between the Fr_s number based on mixture velocity and the Fr_{TB} number based on Taylor bubble velocity, which is gained by the conductivity probes and digital high-speed video system. The range of Re_s is from 6000 to 66,000. Using least square method, a correlation is obtained as follows:

$$Fr_{TB} = 1.217Fr_s + 0.35 \tag{15}$$

It has been found that the experimental results are in good agreement with the results predicted by Nicklin's formula with a maximum deviation of 4%, although the liquid surface tension and viscosity are much smaller than those of the pure water used in the Nicklin's experiments, which indicates that Taylor bubble velocity is not sensitive to the change of liquid viscosity and surface tension, namely the regime is inertia controlled, the fluid is considered to be inviscid and surface tension effect is negligible, which can be explained by the potential flow theory except the falling liquid film far away from the Taylor bubble nose.

In previous experimental and theoretical research, great endeavor has been devoted to the accurate determination of Taylor bubble shape. For sufficiently long bubbles, the Taylor bubble nose shape was observed to be spherical and independent of the bubble length, whereas there is a more or less deviation from spherical cap for most bubbles in practice. Aladjem Talvy et al. (2000) found that strong deformation and oscillations of the succeeding Taylor bubble nose were observed and that the oscillations are related to the quasi-resonant oscillations of the leading bubble bottom. Previous research was mainly focused on the effect of surface tension on the Taylor bubble shape in stagnant liquid, and the effects of superficial velocities were neglected. Brown (1965) measured the rise of Taylor bubbles in liquids with different viscosities, and proposed a universal expression for the nose radius of curvature, i.e., $R_0 = 0.75R_c$, where $R_c = R - \delta_t$ (δ_t is the terminal thickness of the liquid film). Collins and de Moraes (1978) measured the radius of curvature of bubble nose by photographing the propagating bubbles, and found that the radius of curvature tends to decrease with increased liquid velocity. According to the potential flow theory, the radius of curvature R_c of Taylor bubble nose can be expressed as follows:

$$\begin{aligned} \frac{R_c}{R} &= \frac{4\beta_1}{\beta_1^2 + 4k_1\frac{U_c}{U_0}} \\ k_1 &= 7.5[4.12 + 4.95(\log Re - 0.743)]^{-1} \\ Re &= \frac{\rho_L D U_s}{\mu_L} \end{aligned} \tag{16}$$

where $\beta_1 = 3.8317$, which is the first order positive zero point of Bessel function. U_c is the velocity of the liquid in front of Taylor bubble nose and U_0 is the drift velocity.

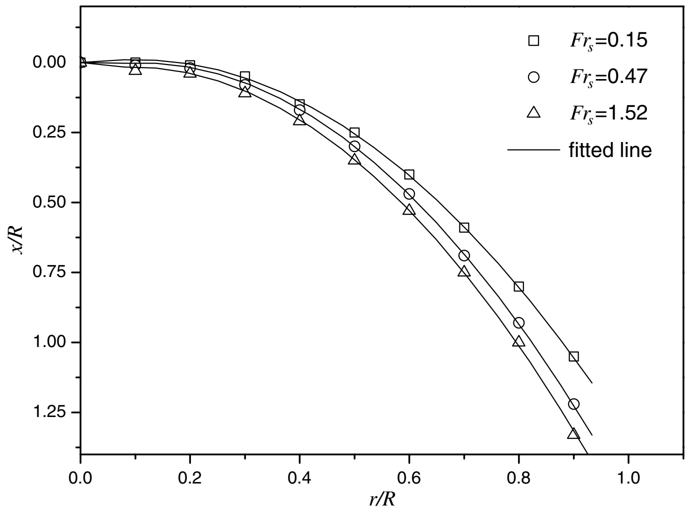

Fig. 6. The stable Taylor bubble nose shape.

Fig. 6 shows the experimental results of the Taylor bubble nose shape at different values of Fr_s. It can be seen that the radius of curvature of Taylor bubble nose is reduced with increased Fr_s, which is consistent with Collins' results. The Taylor bubble nose radius of curvature is $R_0 = 0.71R_c$, smaller than Brown's results, which may be caused by the difference in experimental conditions. The Taylor bubble shape is measured in the flowing liquid whereas Brown's results were obtained in a stagnant liquid. Fig. 7 shows the comparisons of normalized radius of curvature between the results by Eq. (16) and by experiments. It can be noted that the predicted results are always higher than the experimental results, which is caused for the most part by the first-order approximation of the Bessel function. Moreover, by using the digital high-speed video system, it has been found that the Taylor bubble nose shape does not depend on the bubble length and the Taylor bubble bottom has a concave shape, which is essentially insensitive to the superficial velocities and the bubble length.

3.1.2. Falling liquid film

The parameters associated with the falling liquid film become crucial for the modeling of slug flow induced corrosion. For instance, the intensity of the vortices in the liquid slug may be closely related to the velocity of

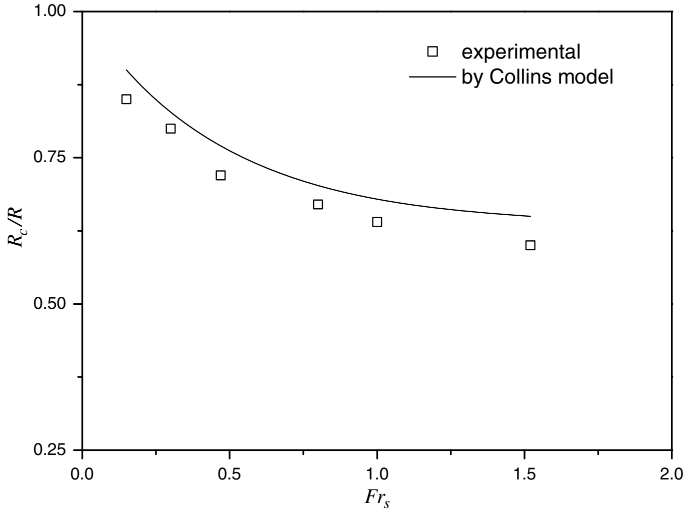

Fig. 7. Normalized radius of curvature comparisons between the results by Eq. (16) and by experiments.

the falling liquid film at the bottom of the Taylor bubble, which is the function of the film thickness. Moreover, the falling liquid film flow characteristics play a key role in the flow induced corrosion. The hydrodynamic boundary layer and diffusion boundary layer on the metal substrate surface, the mass transfer of corrosive reactants and corrosion products, the electrochemical corrosion reaction process, the applied alternating shear stress on the corrosion product film, and also the processes of corrosion product film's formation, damage and repair, are all distinctly affected by the falling liquid film.

Previous experimental results have validated that the annular falling film around the Taylor bubble can be assumed to be a liquid film without interfacial shear, namely the flow characteristics of falling liquid film in the Taylor bubble nose zone obey the potential flow theory and the Taylor bubble nose is a spherical cap, but this assumption is inappropriate to the bottom of the Taylor bubble.

According to the potential flow theory, Davies and Taylor (1950) suggested a relationship for the thickness of the falling liquid film

$$\eta - \eta^2 = \frac{0.0583}{\sqrt{\xi}} \tag{17}$$

where $\eta = \delta/D$ is the dimensionless falling liquid film thickness, and $\xi = x/D$ is the dimensionless axial distance from the Taylor bubble nose. Nevertheless, Ozgu et al. (1973) took into account the effect of viscosity and the hydrodynamic characteristics, and gave a modification for the Davies and Taylor's relationship as follows:

$$\text{For the falling liquid film in the laminar flow, } \eta' = \frac{\eta}{0.667} \tag{18}$$

$$\text{For the falling liquid film in the turbulent flow, } \eta' = \frac{\eta}{0.656} \tag{19}$$

where η is the modified dimensionless falling liquid film thickness.

Fig. 8 shows the dimensionless falling liquid film thicknesses both by the experiments and by Eqs. (17) and (19). From the experimental results, it can be seen that at the Taylor bubble nose zone $x/D < 0.75$ the developing falling liquid film thins as it falls, and the thickness of which at high superficial gas velocity is larger than that at the low superficial gas velocity, which can be considered to be attributed to the smaller radius of curvature at the high superficial velocity. When $x/D < 0.75$, the results by Eq. (17) are close to the experimental results, which verifies that the flow characteristics of the developing falling liquid film can be explained by the potential flow theory at the Taylor bubble nose zone. However, at $x/D > 0.75$, the fully developed falling liquid film is eventually reached, and the thickness of which at high superficial gas velocity is smaller than that at low superficial gas velocity, and the model results have an obvious deviation from the experimental results.

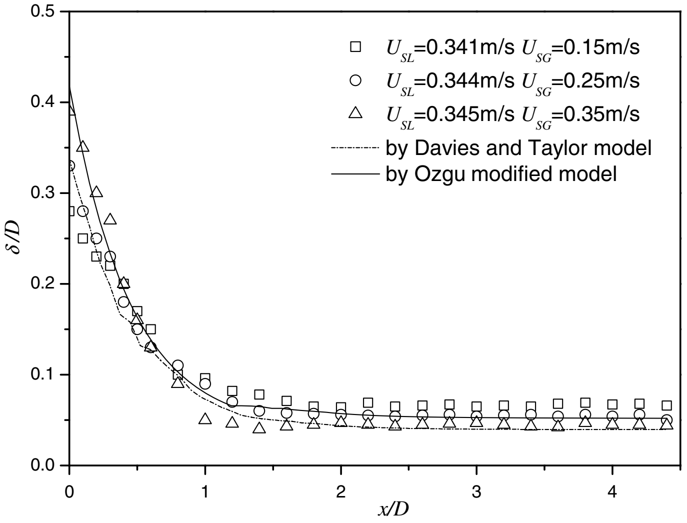

Fig. 8. Dimensionless falling liquid film thicknesses by experiments and by predicting models.

In the model, only δ, x, and D are correlated, and all other possible influential factors are reflected by the constant 0.0583, at least the relationship between the thickness and the velocity of the falling liquid film is not clear, resulting in the difficulty for the predicting model to be appropriate for the falling liquid films under all flow conditions. The Ozgu model improves the predicted results in the Taylor bubble bottom zone, as shown in Fig. 8. But this modified model is still unable to overcome the shortcomings of the Davies and Taylor model.

Brotz (1954) proposed an empirical correlation for the thickness of free falling liquid film by studying water, pentadecane and refrigerating oil in turbulent flows in different diameter tubes as follows:

$$\delta_{\mathrm{L}}\left(\frac{g}{v_{\mathrm{L}}^2}\right)^{1/3} = \left(\frac{3Re_{\mathrm{f}}^2}{590}\right)^{1/3} \tag{20}$$

$$Re_{\mathrm{f}} = \frac{\delta_{\mathrm{L}} U_{\mathrm{f}}}{v_{\mathrm{L}}} \tag{21}$$

where δ_{L} is the mean liquid film thickness, v_{L} the liquid kinematical viscosity. Substituting Eq. (21) into Eq. (20) gives

$$U_{\mathrm{f}}^2 = 196.7 g \delta_{\mathrm{L}} \tag{22}$$

δ_{L} can be related to the void fraction of the Taylor bubble $\langle \alpha_{\mathrm{TB}} \rangle$ by

$$\delta_{\mathrm{L}} = 0.5D\left(1 - \sqrt{\langle \alpha_{\mathrm{TB}} \rangle}\right) \tag{23}$$

Thus

$$U_{\mathrm{f}} = 9.916\left[gD(1 - \sqrt{\langle \alpha_{\mathrm{TB}} \rangle})\right]^{0.5} \tag{24}$$

For the sufficiently long Taylor bubbles, the length of falling liquid film is 30–100 times the mean film thickness for most of steady slug flows. The gravitational force acting on the film balances the wall shear force, which makes the falling liquid film attain a terminal thickness δ_{t} and a terminal velocity U_{ft}. Wallis (1969) gave a formula as follows:

$$\frac{\delta_t}{D} = k\left[\frac{\mu_{\mathrm{L}}^2}{D^3 g(\rho_{\mathrm{L}} - \rho_{\mathrm{G}})\rho_{\mathrm{L}}}\right]^{1/3}\left(\frac{4\Gamma}{\mu_{\mathrm{L}}}\right)^m \tag{25}$$

$\Gamma = \rho_{\mathrm{L}}|U_{\mathrm{ft}}|\delta_{\mathrm{t}}$, is the mass flow rate per a peripheral length unit. For laminar flows, $Re_{\mathrm{f}} = 4\Gamma/\mu_{\mathrm{L}} < 1000$, Wallis suggested $k = 0.909$ and $m = 1.3$; for turbulent flows, $Re_{\mathrm{f}} = 4\Gamma/\mu_{\mathrm{L}} > 1000$, Wallis suggested $k = 0.115$ and $m = 0.6$.

Fig. 9 shows the velocity of falling liquid film along the Taylor bubble. The velocity of falling liquid film is increased with increased superficial gas velocity. The experimental results for the mean thickness and velocity of falling liquid film are in better agreement with the predicted results by Brotz model. Whereas the terminal thickness δ_{t} and the terminal velocity U_{ft} of falling liquid film are best fitted with $k = 0.103$ and $m = 0.64$ for the turbulent flows ($Re_{\mathrm{f}} > 650$). Compared with Wallis model, the differences in k and m may be caused by the different physical properties of fluids.

Due to the pseudo-periodicity for an upward fully developed slug flow, there are many complicated hydrodynamic characteristics appearing in the near wall zone, as shown in Fig. 10. When the falling liquid film is formed at the Taylor bubble nose and runs down all the way to the Taylor bubble bottom, the film velocity is downward and has an increasing magnitude. When the falling liquid film plunges into the wake of Taylor bubble, meeting the upward bulk liquid flow, the film velocity is downward and decreases to zero until the falling film is fully assimilated by liquid slug. Then the fluid near the wall starts to flow upward and the velocity increases until the succeeding Taylor bubble comes. Henceforth, a falling liquid film is formed at the succeeding Taylor bubble nose.

In the Taylor bubble wake, when the falling liquid film plunges into the liquid rising behind the bubble, small bubbles will be entrained and then shed off, as shown in Fig. 11. Since the space in the wake is confined, when the falling liquid film plunges into the wake, the falling liquid film goes through a transition from a

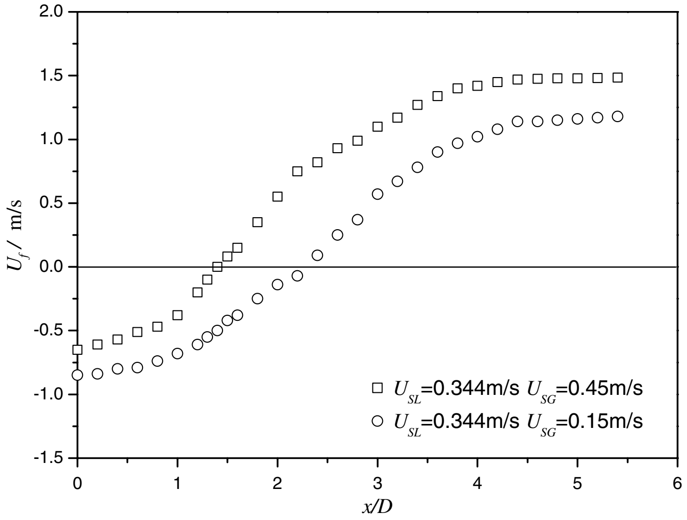

Fig. 9. Velocity of falling liquid film along Taylor bubble.

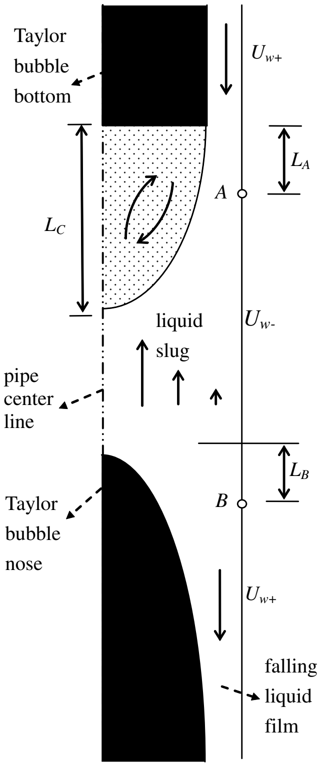

Fig. 10. Schematic map of the velocity change in the near wall zone for an upward slug flow.

smooth free surface to a rough surface, generating a gravity wave, which induces a transverse wave and a longitudinal wave. The oscillation is apt to lead to an enclosed cavity, with many spiral vortexes in various sizes, and small bubbles entrained in it. The distortion of the Taylor bubble bottom and the fluctuation of the liquid surface will induce the entrained bubbles to shed off from the wake of Taylor bubble and enter the succeeding liquid slug.

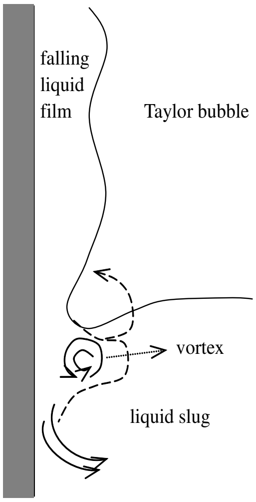

Fig. 11. Entrainment and shedding-off at the bottom of the Taylor bubble.

Previous research shows that the wake region is in a free turbulence and the falling liquid film can be regarded as a two-dimensional liquid ring jet entering a stagnant liquid slug pool (Taitel et al., 1980). As the falling liquid film moves downward and the Taylor bubble moves upward, the jet velocity in the wake of Taylor bubble where the jet is entering the stagnant liquid slug pool can be expressed as

$$U_{\mathrm{jet}} = U_{\mathrm{f}} + U_{\mathrm{TB}} \tag{26}$$

The axial velocity in the wake region can be expressed by the following (Ghosh and Cui, 1999):

$$U_{\mathrm{axial}} = U_{\mathrm{jet}}[1 - \tanh^2(7.67y/x)] \tag{27}$$

where x is the direction along the jet and y is the direction perpendicular to the jet. When $x = L_{\mathrm{C}}$, $y = 0.5D$, $U_{\mathrm{axial}} = 0$, as shown in Fig. 10. The averaged axial velocity in the wake region can be determined as

$$\langle U_{\mathrm{axial}} \rangle = \frac{U_{\mathrm{jet}} \int_{0^+}^{L_{\mathrm{C}}} \int_0^{0.5D} [1 - \tanh^2(7.67y/x)]\, \mathrm{d}y\, \mathrm{d}x}{\int_{0^+}^{L_{\mathrm{C}}} \int_0^{0.5D} \mathrm{d}y\, \mathrm{d}x} \tag{28}$$

For a fully developed slug flow, the Taylor bubble length remains constant, and the fluxes of gas entering and leaving the Taylor bubble must be equal. Namely

$$Q_{\mathrm{a}} + Q_{\mathrm{b}} = Q_{\mathrm{c}} \tag{29}$$

where Q_{a}, Q_{b} and Q_{c} are the fluxes of gas entering the Taylor bubble at the nose, re-coalescence to the Taylor bubble across its bottom plane, and entrainment by the falling liquid film respectively.

Using the model proposed by Fernandes et al. (1983), in our experimental conditions, it is found that the entrainment flux Q_{c} is in the range from $1.12Q_{\mathrm{a}}$ to $1.31Q_{\mathrm{a}}$. Using the digital high-speed video system, it is found that most of small bubbles carried by the falling liquid film at the Taylor bubble nose do not coalesce into the Taylor bubble, are running down all the way, and eventually fully plunge into the liquid slug, which is quite different from air–water two-phase upward slug flow. The difference may be attributed to the fact that the electrolytic solution tends to foam more easily and the small bubbles are more stable due to lower surface tension.

When a falling liquid film passes by a Taylor bubble into the wake, there exists an issue of penetration distance, as shown in Fig. 10. The penetration distance is decreased with increased superficial gas velocity. Nevertheless, the penetration distance is increased with increased superficial liquid velocity. When the length of liquid slug is less than penetration distance, at the constant superficial liquid velocity, the falling liquid film holds an annular space, leading to an increase of upward velocity of liquid, and the succeeding Taylor bubble rise velocity can also be increased. However, the penetration distance of the falling liquid film has no effect on

Table 2
The length change in the near wall zone for an upward slug flow unit

U_{SG} (m/s)	U_{SL} (m/s)	L_A (D)	L_B (D)	L_C (D)
0.15	0.344	2.08	0.57	3.04
0.25	0.344	1.55	0.61	2.38
0.35	0.344	1.17	0.78	1.85
0.45	0.344	0.71	0.85	1.28
0.15	0.446	2.41	0.56	3.54
0.25	0.446	1.71	0.60	2.63
0.35	0.446	1.28	0.76	2.02
0.45	0.446	0.89	0.82	1.59
0.15	0.518	2.67	0.54	3.91
0.25	0.518	1.89	0.59	2.91
0.35	0.518	1.37	0.73	2.17
0.45	0.518	0.99	0.8	1.77
0.15	0.651	2.83	0.51	4.16
0.25	0.651	2.04	0.54	3.13
0.35	0.651	1.50	0.66	2.38
0.45	0.651	1.06	0.76	1.90

the succeeding Taylor bubble when the liquid slug length is greater than the penetration distance. In the experiments, it is found that the penetration length L_A and the Taylor bubble wake length L_C accounts respectively for 10–15% and 18–23% of the liquid slug length L_{LS}. The falling liquid film is formed at the distance of 0.5–1.1D from the Taylor bubble nose in all experiments.

Table 2 shows the distributions of the penetration length L_A, the Taylor bubble wake length L_C, and the falling liquid film formation distance from the Taylor bubble nose L_B.

3.2. Flow characteristics in liquid slug zone

Using the high-speed video system, it is found that liquid slug consists of three parts. The first part is the wake region of the leading Taylor bubble that assimilates the falling liquid film, which is extremely turbulent, disorderly and chaotic with maximum void fraction. The bubbles torn from the Taylor bubble cause the wake vortices. In this part, the liquid carrying dispersed small bubbles flows downward in the near wall zone, whereas liquid flows upward in the core of pipe. The second part is regarded as the transition region from the wake to the fully developed dispersed bubble region. In this part, the bubbles come from the core area of the wake region and then gradually spread across the entire cross section of pipe. The third part is defined as the minimum void fraction region, which may be either turbulent or laminar. In this part, the void fraction distribution is very similar to that of fully developed dispersed bubble flow.

Aladjem Talvy et al. (2000) found that the succeeding Taylor bubble dose not affect the motion of the leading one and is sensitive to the velocity distortion in the wake of the leading bubble. The succeeding bubble acceleration is quite prominent in the near wake of the leading elongated bubble. However, for a fully developed upward slug flow, an important parameter that attention should be paid to is the minimum stable liquid slug, namely the minimum distance for restoring a fully developed velocity distribution in the liquid slug. Moissis and Griffith (1962) concluded by experiments that a certain separation distance between the two bubbles is needed to have fully developed conditions and suggested this distance should be about 8–16D for air–water systems. Theoretical reasoning for the minimum stable liquid slug length was carried out by Taitel et al. (1980), Dukler et al. (1985) and Shemer and Barnea (1987). It has been found that the minimum stable liquid slug length is relatively insensitive to the gas and liquid flow rate, and is fairly constant for a given pipe diameter.

Fig. 12 shows the relationship between dimensionless velocity $(Fr_{TB} - Fr_0)/Fr_s$ and liquid slug length at different superficial gas and liquid velocities, it is also verified that the minimum stable liquid slug length is constant and about 7.5–10D.

Using digital high-speed video system, the dispersed bubble size in liquid slug is also investigated. Fig. 13 shows the dispersed bubble size distribution in liquid slug, N_d is the number of the sample bubbles with certain

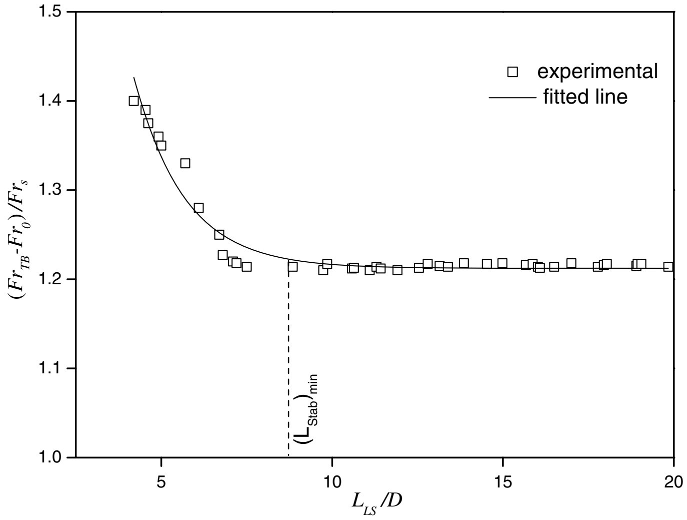

Fig. 12. The relationship between dimensionless velocity and liquid slug length.

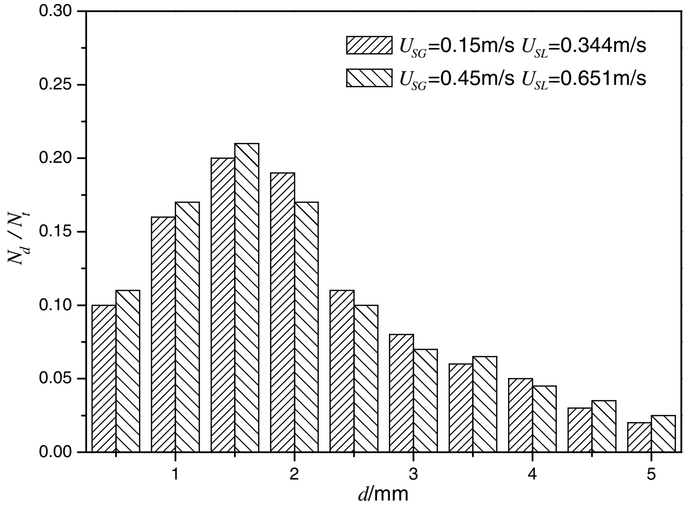

Fig. 13. Dispersed bubble size distribution in liquid slug.

characteristic diameter, N_t the total number of the investigated sample bubbles and N_d/N_t the fraction of the bubbles with a given characteristic diameter. It is found that the diameters of the dispersed bubbles are within 5.5 mm, and the bubbles with about 1.5–2.5 mm diameter account for 75%. It is also found that the bubbles which appear in fully developed dispersed liquid slug are within 1.5 mm diameter and close to be spherical. Whereas the bubbles which appear in the wake of Taylor bubble are above 1.5 mm diameter and more or less distorted.

According to previous research, the averaged bubble rise velocity U_{GLS} in the liquid slug in the fully developed dispersed bubbly flow is the sum of the average liquid velocity of the liquid slug U_{LLS} and the bubble buoyancy velocity, U_0. Hence

$$U_{GLS} = U_{LLS} + U_0 \tag{30}$$

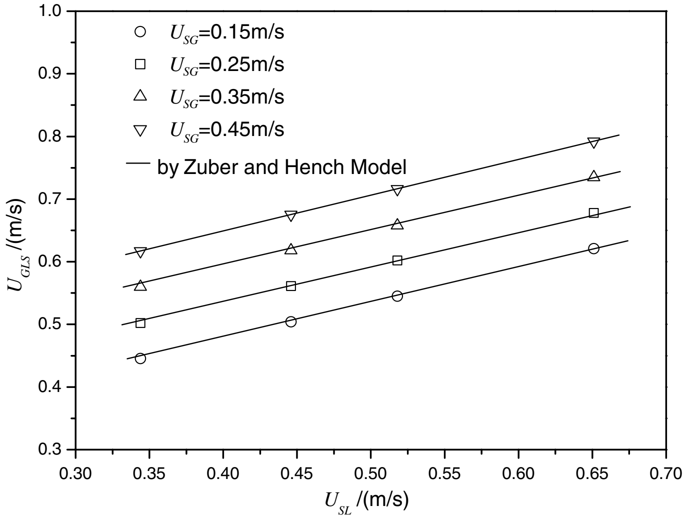

Fig. 14. Dispersed bubble velocity in liquid slug.

For a single bubble, Harmathy (1960) suggested

$$U_0 = 1.53\left[\frac{\sigma g(\rho_L - \rho_G)}{\rho_L^2}\right]^{1/4} \tag{31}$$

where σ is the gas–liquid interfacial tension.

For a bubbles swarm, Zuber and Hench (1962) found that U_0 is dependent on the $\langle\alpha_{LS}\rangle$ and proposed the following expression

$$U_0 = 1.53\left[\frac{\sigma g(\rho_L - \rho_G)}{\rho_L^2}\right]^{1/4}(1 - \langle\alpha_{LS}\rangle)^{1/2} \tag{32}$$

It can be seen that when the void fraction increases, U_0 decreases.

Fig. 14 shows the dispersed bubble velocity in liquid slug, it is found that the experimental results are fitted well with the model proposed by Zuber and Hench (1962). At the constant superficial gas velocity, the bubble velocity in liquid slug is increased with increased superficial liquid velocity. At a constant superficial liquid velocity, the bubble velocity in liquid slug is also increased with increased superficial gas velocity, but more slowly. This can be explained as follows: when the superficial liquid velocity increases, U_{LLS} increases and U_0 increases due to decreased $\langle\alpha_{LS}\rangle$. However, as the superficial gas velocity increases, U_0 decreases due to increased $\langle\alpha_{LS}\rangle$, but U_{LLS} increases.

In the gas–liquid slug flow, the intermittence of Taylor bubble and liquid slug is an essential characteristic. The intermittent flow is one of the important factors to induce the fatigue stress cracking of the corrosion production film in the near wall zone in a system under corrosion. The intermittence of slug flow can be characterized by liquid slug frequency

$$f_s = \frac{N_{SU}}{\Delta t} \tag{33}$$

where N_{SU} is the number of slug units at time interval Δt.

Fig. 15 shows the liquid slug frequency distribution at different superficial gas and liquid velocities. It is indicated that the liquid slug frequency is generally above 2 Hz, and the liquid slug frequency increases with increased superficial liquid velocity, whereas the liquid slug frequency decreases with increased superficial gas velocity.

3.3. Length distribution and void fraction characteristics of slug unit

Taylor bubble length L_{TB} and liquid slug length L_{LS} are the primary elements in studying the hydrodynamic characteristics of upward slug flow. The length fraction of Taylor bubble β is defined as

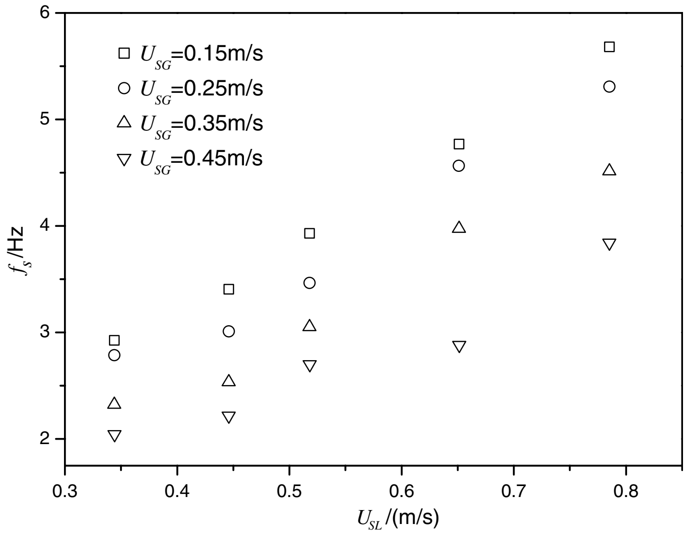

Fig. 15. Liquid slug frequency distribution at different superficial gas and liquid velocities.

$$\beta = \frac{L_{\mathrm{TB}}}{L_{\mathrm{SU}}} = \frac{L_{\mathrm{TB}}}{L_{\mathrm{TB}} + L_{\mathrm{LS}}} \tag{34}$$

Figs. 16–18 show the results of Taylor bubble length L_{TB}, liquid slug length L_{LS} and Taylor bubble length fraction β at different superficial velocities, respectively. With the increase of superficial gas velocity at a given superficial liquid velocity, L_{TB} and β are evidently increased, whereas the liquid slug length L_{LS} is decreased. With increased superficial liquid velocity at a given superficial gas velocity, liquid slug length L_{LS} is increased and β is decreased, moreover as the superficial gas velocity is further decreased, the decrease of β is slowed down.

Figs. 19 and 20 show the distributions of the Taylor bubble length L_{TB} and the liquid slug length L_{LS} at different superficial gas and liquid velocities, where N_{TB} and N_{LS} are the numbers of the sample Taylor bubbles and liquid slugs with certain dimensionless length, N_{TBt} and N_{LSt} the total number of the sample Taylor bubbles and liquid slugs, $N_{\mathrm{TB}}/N_{\mathrm{TBt}}$ and $N_{\mathrm{LS}}/N_{\mathrm{LSt}}$ the fractions of the Taylor bubbles and liquid slugs

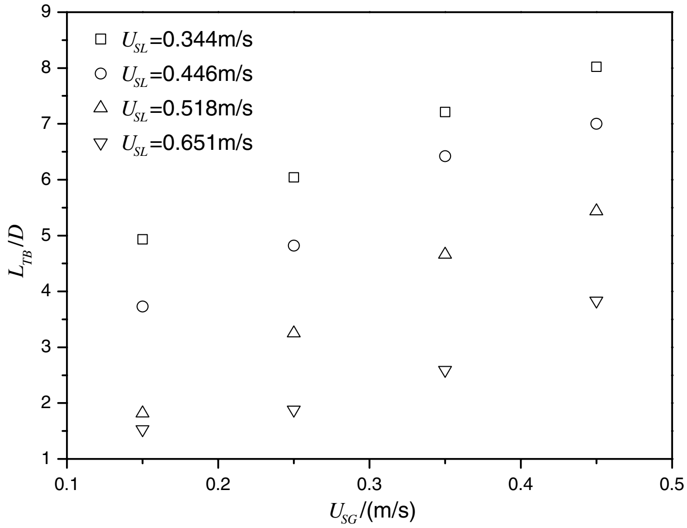

Fig. 16. Taylor bubble length L_{TB} distribution at different superficial gas and liquid velocities.

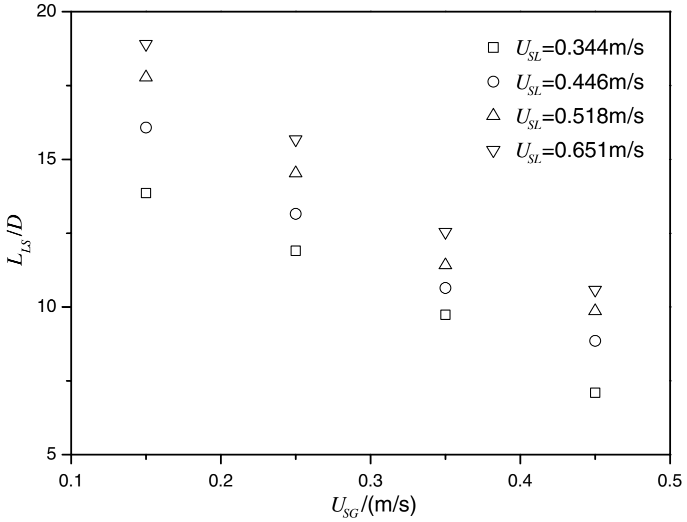

Fig. 17. Liquid slug length L_{LS} distribution at different superficial gas and liquid velocities.

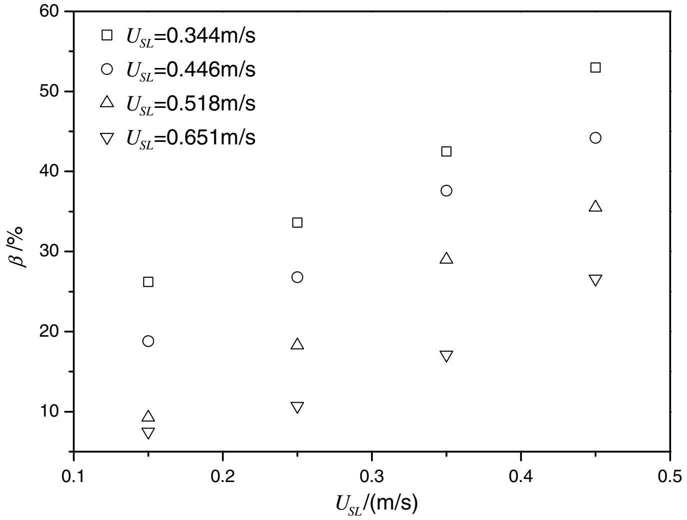

Fig. 18. Taylor bubble length fraction β distribution at different superficial gas and liquid velocities.

with a given dimensionless length, respectively. It can be seen that the mean length L_{TBmean}, the minimum length L_{TBmin} and the maximum length L_{TBmax} of Taylor bubble are all increased with the increase of superficial gas velocity. Whereas the mean length L_{LSmean}, the minimum length L_{LSmin} and the maximum length L_{LSmax} of liquid slug are all increased with the increase of superficial liquid velocity. It is found that short Taylor bubble and short liquid slug exist under all experimental conditions, and the shorter Taylor bubbles are prone to coalesce into larger Taylor bubble, which also has been found by van Hout et al. (2001). The distribution characteristics of both the Taylor bubble length L_{TB} and the liquid slug length L_{LS}, which exhibit a little skewness, but not so significantly as the results of van Hout et al. (2001), fitted well to the normal distribution shape depicted by the solid lines in Figs. 19 and 20. The probability density function of the normal distribution is

$$f(L_i/D|\mu_i,\sigma_i) = \frac{1}{\sqrt{2\pi}\sigma_i}\exp-\left(\frac{L_i/D-\mu_i}{\sqrt{2}\sigma_i}\right)^2 \tag{35}$$

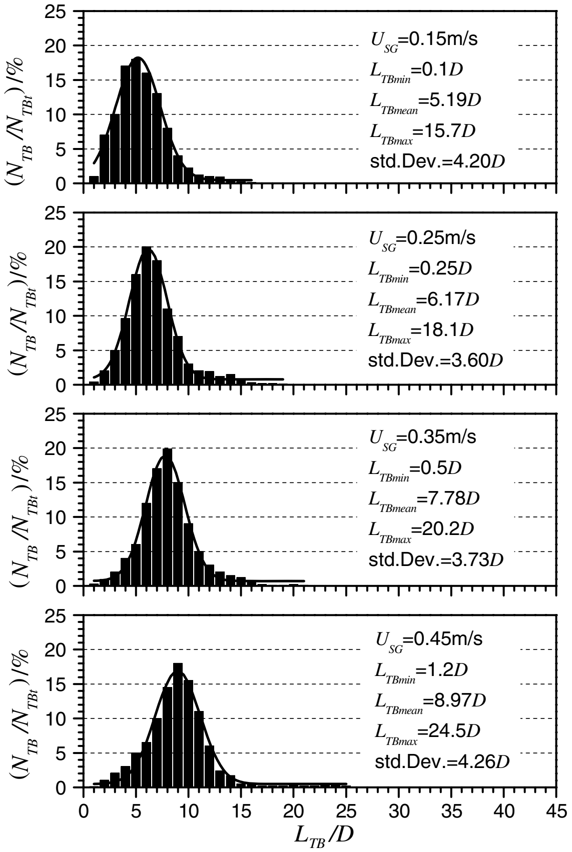

Fig. 19. Taylor bubble length L_{TB} distribution at different superficial gas velocities with constant superficial liquid velocity $U_{SL} = 0.344$ m/s.

where L_i/D is the dimensionless length of Taylor bubble length L_{TB} or the liquid slug length L_{LS}, μ_i their mean length $L_{i\text{mean}}$ and σ_i their standard deviation (std. dev.).

Void fraction for slug unit and liquid slug represents the two-phase spatial distribution, which is an important parameter in modeling the slug flow. The intermittence characteristics of the Taylor bubble with high void fraction and the liquid slug with small void fraction give rise to the significant difference of the slug flow from other flow regimes. Fig. 21 shows the radial void fraction distribution of slug unit. At low superficial gas velocities, the void fraction of slug unit is in a parabolic curve distribution. With the increase of the superficial gas velocity, the void fraction increases and gets even in the core. At the low superficial gas and liquid velocities, such as the $U_{SL} = 0.344$ m/s and $U_{SG} = 0.152$ m/s, $U_{SL} = 0.446$ m/s and $U_{SG} = 0.248$ m/s, the void fraction in the near wall zone around $r/R = 0.875$ looks like a saddle, similar to the distribution of fully dispersed bubble flow, which means the flow is unstable and goes through flow regime transition between slug flow and dispersed bubble flow, whereas in the core of pipe, there is a gibbosity of void fraction, which implies that large Taylor bubbles tend to be in the core of pipe. As the superficial liquid velocity increases, the void fraction becomes decreased with even profile in the core. Moreover, the parabolic curve and the saddle shape distribution disappear.

Fig. 22 shows the radial void fraction distribution of liquid slug, which is shaped like a saddle. In the range of 0–0.75R, the void fraction is decreased with increased r. Nevertheless, in the range of 0.75–1R, the void fraction increases sharply, around 0.80–0.90R, a peak value appears, and then the void fraction decreases to zero at the wall (1R). With the increase of superficial gas velocity, the void fraction increases and becomes even in the core, and the peak value in the near wall zone moves toward the wall, the results are similar to those of Nakoryakov and Kashinsky (1981). The void fraction in the core of pipe is below 0.35, since the many dispersed bubbles will coalesce into the leading Taylor bubble when the void fraction above 0.35. Liu and

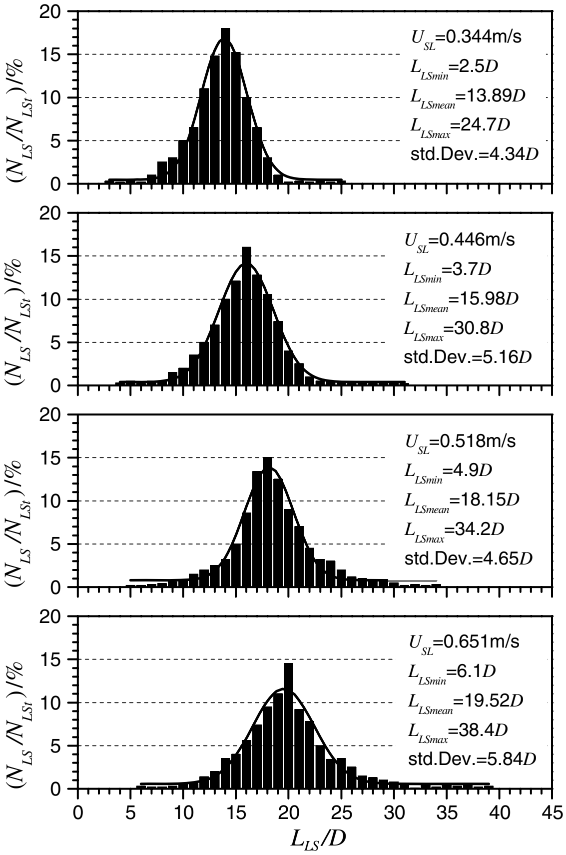

Fig. 20. Liquid slug length L_{LS} distribution at different superficial liquid velocities with constant superficial gas velocity $U_{SG} = 0.15$ m/s.

Bankoff (1993) investigated the air–water bubbly flow structure in a vertical pipe, and found that the void fraction is below 0.35, which justifies that the void fraction distribution in liquid slug is similar to that in a fully developed dispersed bubble flow. Moreover, with the increase of superficial liquid velocity, the void fraction radial distribution in liquid slug decreases to a little invariable distribution and the effect of superficial gas velocity on it is reduced, namely at high superficial liquid velocity, the void fraction radial distribution is insensitive to the change of superficial gas velocity, which can be explained by the flow regime transition theory of Taitel et al. (1980). Therefore, the void fraction in liquid slug can be regarded as a fully dispersed bubble flow.

As noted above, the liquid slug consists of three parts, namely the wake region of the leading Taylor bubble, the transition region from the wake to the fully developed dispersed bubble, and the fully developed dispersed bubble region. As shown in Fig. 23, these three regions can be easily distinguished in terms of void fraction distribution. At different superficial velocities, the void fraction profiles in liquid slug are very similar. The void fraction reaches its maximum in the wake region of the leading Taylor bubble with the distance x within 2D. Whereas the void fraction decreases in the transition region with the distance x between 2D and 5D, and the void fraction attains its minimum in the fully dispersed bubble region with the distance x above 6D. The radial void fraction distribution decreases from the maximum at 0.0R to zero at 1.0R in the wake of leading Taylor bubble region. Nevertheless, in the fully dispersed bubble flow, the decreased magnitude of void fraction from 0.0R to 0.75R is small, and then the void fraction increases and achieves a peak value at 0.85R, larger than that at 0.0R. Beyond this, the void fraction decreases and becomes zero at 1.0R. This phenomenon can be explained as follows: in the wake of Taylor bubble, the penetration of falling liquid film causes the radial void fraction to be high at 0.0R and decreases to zero at 1.0R, whereas in the fully dispersed bubble region, the effect of falling liquid film disappears and a fully developed liquid slug velocity profile restores, then the saddle shaped void fraction distribution occurs.

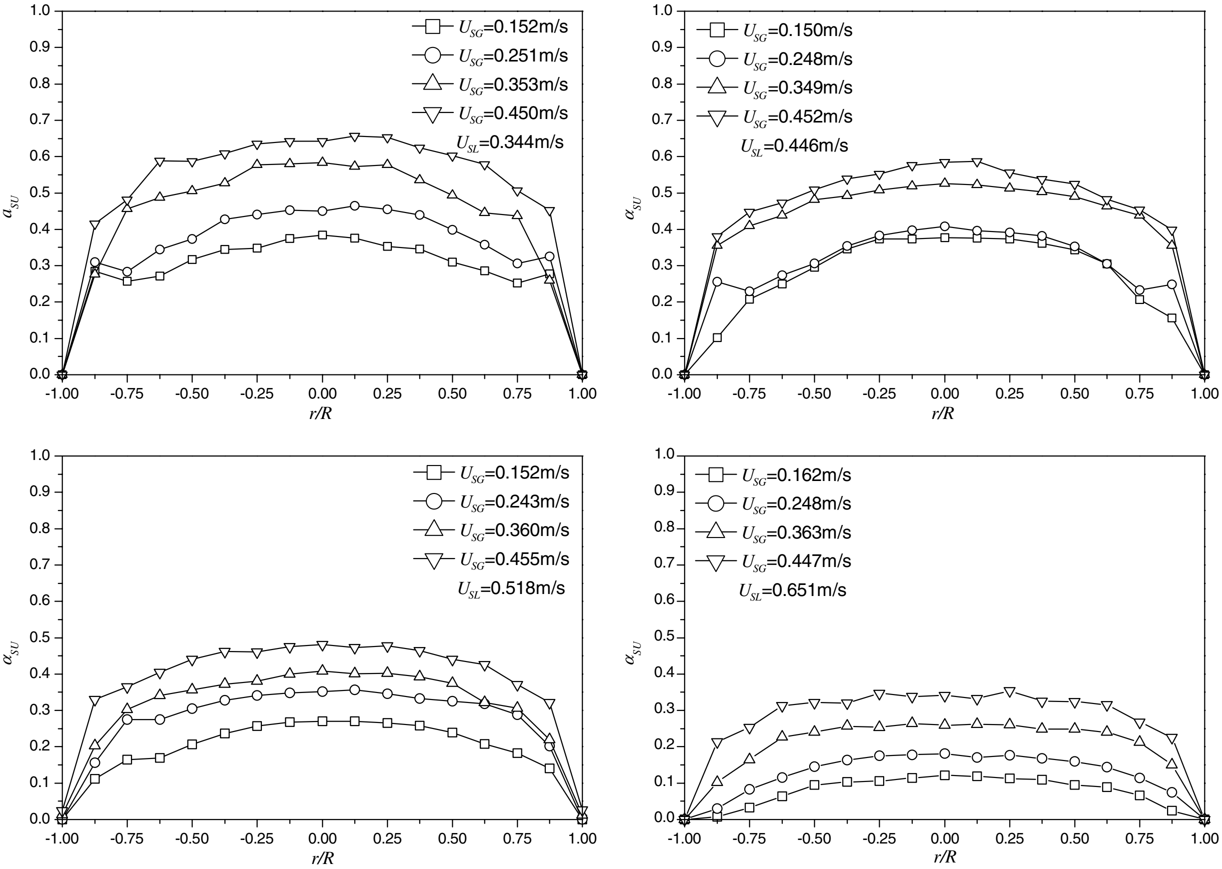

Fig. 21. Slug unit void fraction radial distribution.

Integrating the local radial void fraction distribution can give the averaged void fractions of both slug unit and liquid slug. The results are listed in Table 3. At a given superficial liquid velocity, the void fractions of both slug unit and liquid slug increase with the increase of superficial gas velocity. However, at given superficial gas velocity, the void fractions of both slug unit and liquid slug decrease with increased superficial liquid velocity. Fernandes et al. (1983) found that the averaged void fraction of liquid slug ranges from 0.25 to 0.3, but the average void fraction ranges between 0.05 and 0.26 in the experiments. This may be due to the lower surface tension and viscosity of the solution in the experiments, causing the dispersed bubbles to be more prone to aggregate.

3.4. Instantaneous shear stress and mass transfer in the near wall zone

From the above analyses, it can be found that the upward gas–liquid slug flow induced corrosion is strongly dependent on the turbulent diffusion mass transfer near the wall. The alternate wall shear stress is one of the key factors for the corrosion production film fatigue cracking. The wall shear stress weakens the bonding ability between the metal substrate and the corrosion film, and also causes the destruction of the corrosion film, leading to the exposure of partial or entire metal substrate to the corrosive reactant. The mass transfer is also one of the key factors in the upward gas–liquid slug flow induced corrosion. The turbulent diffusion mass transfer is basically a mixing process. The corrosive reactants are transported from the bulk solution to the reaction surface by the vortex mixing, at the same time, the corrosion productions are transported from the reaction surface to the bulk solution.

Fig. 24 shows the wall shear stress and mass transfer coefficient profiles at different superficial velocities. It can be seen that the wall shear stress and mass transfer coefficient increase with the increase of superficial gas

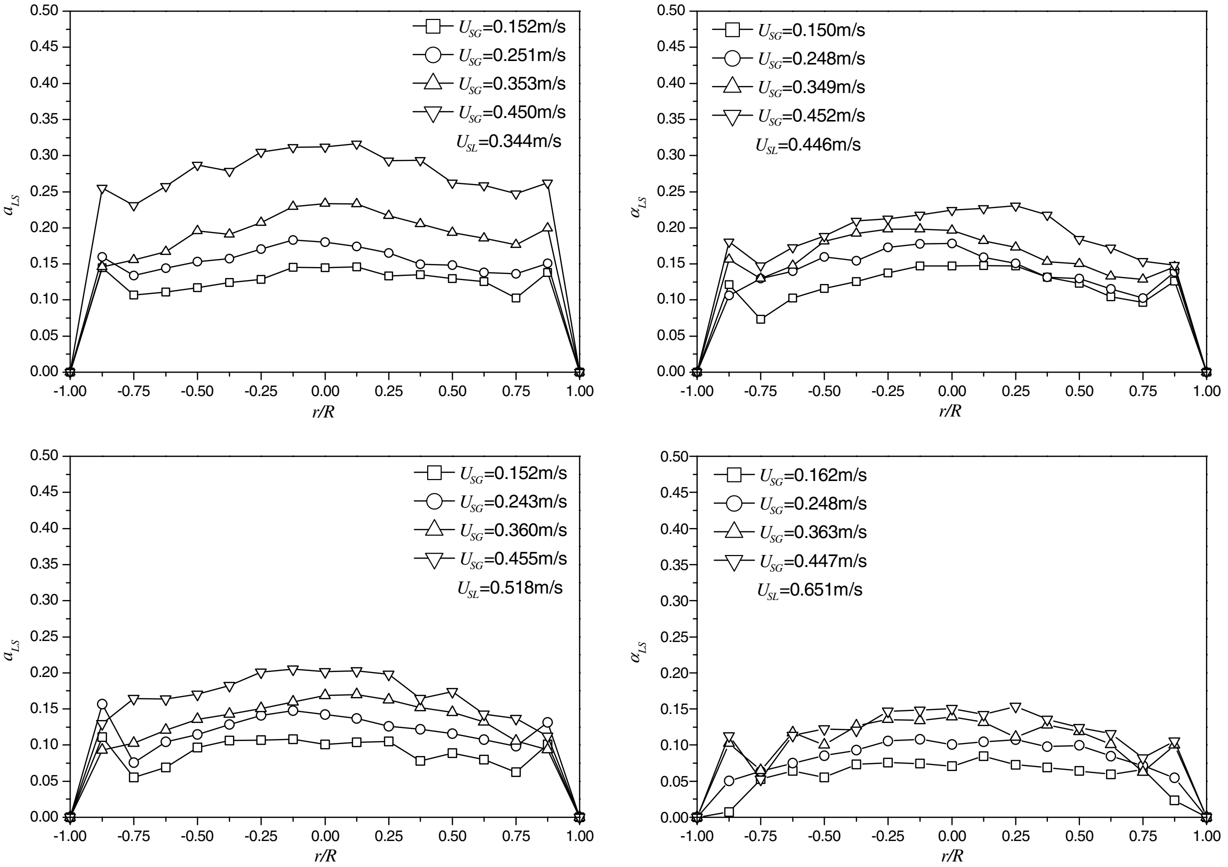

Fig. 22. Liquid slug void fraction radial distribution.

velocity, and decrease with the increase of superficial liquid velocity. When the superficial gas velocity is increased, the falling liquid film terminal velocity is increased and the falling liquid film thickness is reduced, which results in the increase of the velocity gradient and the concentration gradient. When the superficial liquid velocity is increased, the velocity gradient and the concentration gradient decrease. According to the above analyses on the falling liquid film and the liquid slug, and the wall shear stress and mass transfer coefficient distribution characteristics shown in Fig. 24, the near wall zone of upward gas–liquid slug flow can be easily divided into three parts, namely the falling liquid film region corresponding to the length of the Taylor bubble, the Taylor bubble wake region and the remaining liquid slug region.

Previous research shows that the adherence of corrosion product film to the metal substrate is between 10^5 and 10^7 Pa (Schmitt et al., 1999), whereas the wall shear stress of upward gas–liquid slug flow is below 10^3 Pa in all experiments. Therefore, the wall shear stress of upward gas–liquid slug flow is unable to directly damage the corrosion product film. It is the alternate wall shear stress that plays a key role in resultant corrosion production film fatigue cracking.

Of the above three parts, the wake of Taylor bubble is obviously in turbulent flow. The falling liquid film is turbulent except a portion of laminar flow at the Taylor bubble nose where the falling liquid film starts to form, which can be ignored. The fully developed dispersed bubble liquid slug region may be either turbulent or laminar in theory, due to the low viscosity of solution under the experimental conditions, and the fully developed dispersed bubble liquid slug region is also turbulent. Based on the turbulence theory and the rationally corrected single phase mass transfer coefficient formula, the mass transfer coefficients k_{df}, k_{dw} and k_{dLS} respectively in the falling liquid film region, in the wake of Taylor bubble region and in the fully developed dispersed bubble liquid slug region can be expressed as follows:

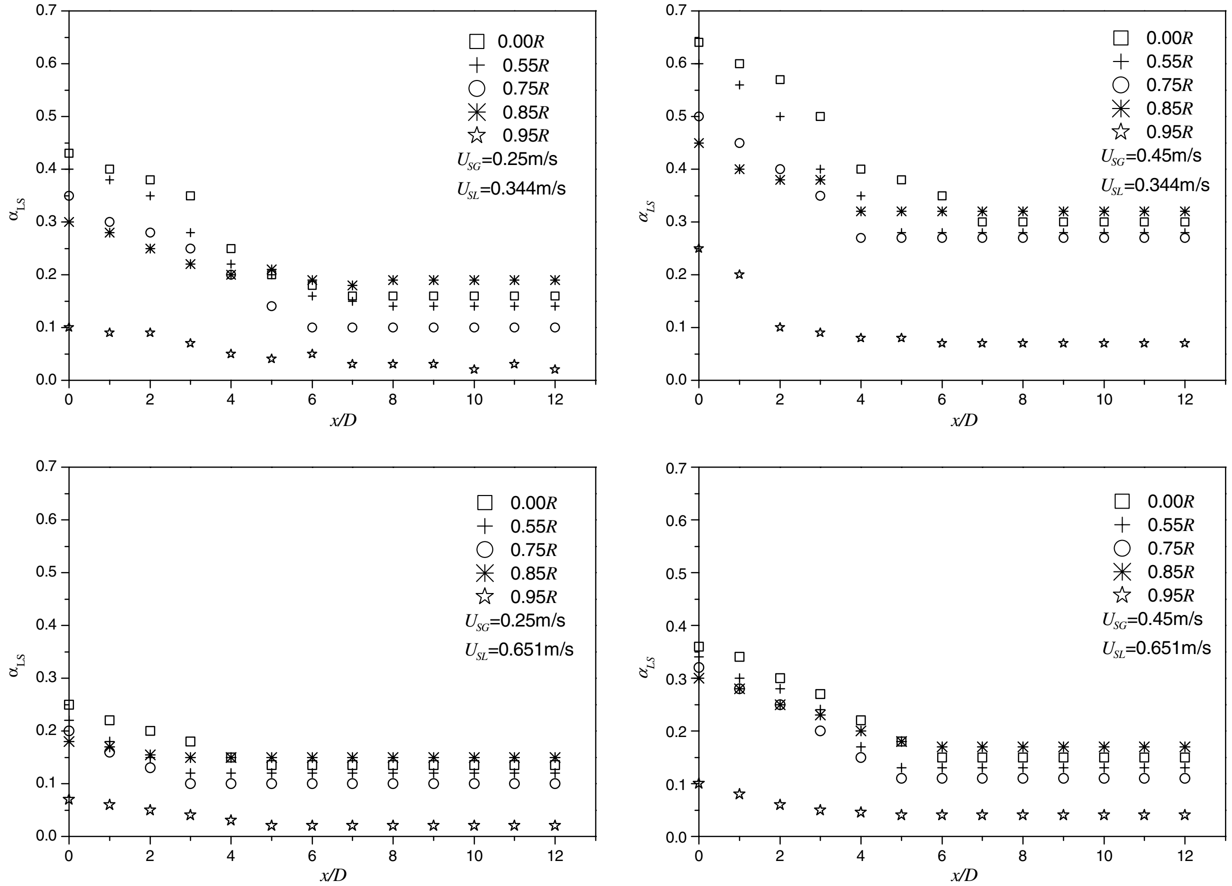

Fig. 23. Radial liquid slug void fraction along the direction of liquid slug length.

Table 3
Averaged void fraction of slug unit $\langle\alpha_{SU}\rangle$ and liquid slug $\langle\alpha_{LS}\rangle$

	$U_{SG} = 0.15$ m/s		$U_{SG} = 0.25$ m/s		$U_{SG} = 0.35$ m/s		$U_{SG} = 0.45$ m/s	
	$\langle\alpha_{SU}\rangle$	$\langle\alpha_{LS}\rangle$	$\langle\alpha_{SU}\rangle$	$\langle\alpha_{LS}\rangle$	$\langle\alpha_{SU}\rangle$	$\langle\alpha_{LS}\rangle$	$\langle\alpha_{SU}\rangle$	$\langle\alpha_{LS}\rangle$
$U_{SL} = 0.344$ m/s	0.299	0.121	0.364	0.146	0.457	0.183	0.542	0.261
$U_{SL} = 0.446$ m/s	0.278	0.115	0.307	0.134	0.438	0.154	0.475	0.18
$U_{SL} = 0.518$ m/s	0.203	0.086	0.284	0.116	0.324	0.127	0.401	0.159
$U_{SL} = 0.651$ m/s	0.079	0.057	0.13	0.081	0.212	0.105	0.287	0.114

$$k_d = 0.023CRe^{0.8}Sc^{0.33}\left(\frac{D_d}{L}\right) = 0.023C\left(\frac{\rho UL}{\mu}\right)^{0.8}\left(\frac{\mu}{\rho D_d}\right)^{0.33}\left(\frac{D_d}{L}\right) \tag{36}$$

where

$$C = 0.27\left(1+\frac{Fr_s}{\beta}\right)^{0.5} \tag{37}$$

The proposed parameters in the formula are shown in Table 4. Good agreement can be found, and the maximum deviation is within ±10%.

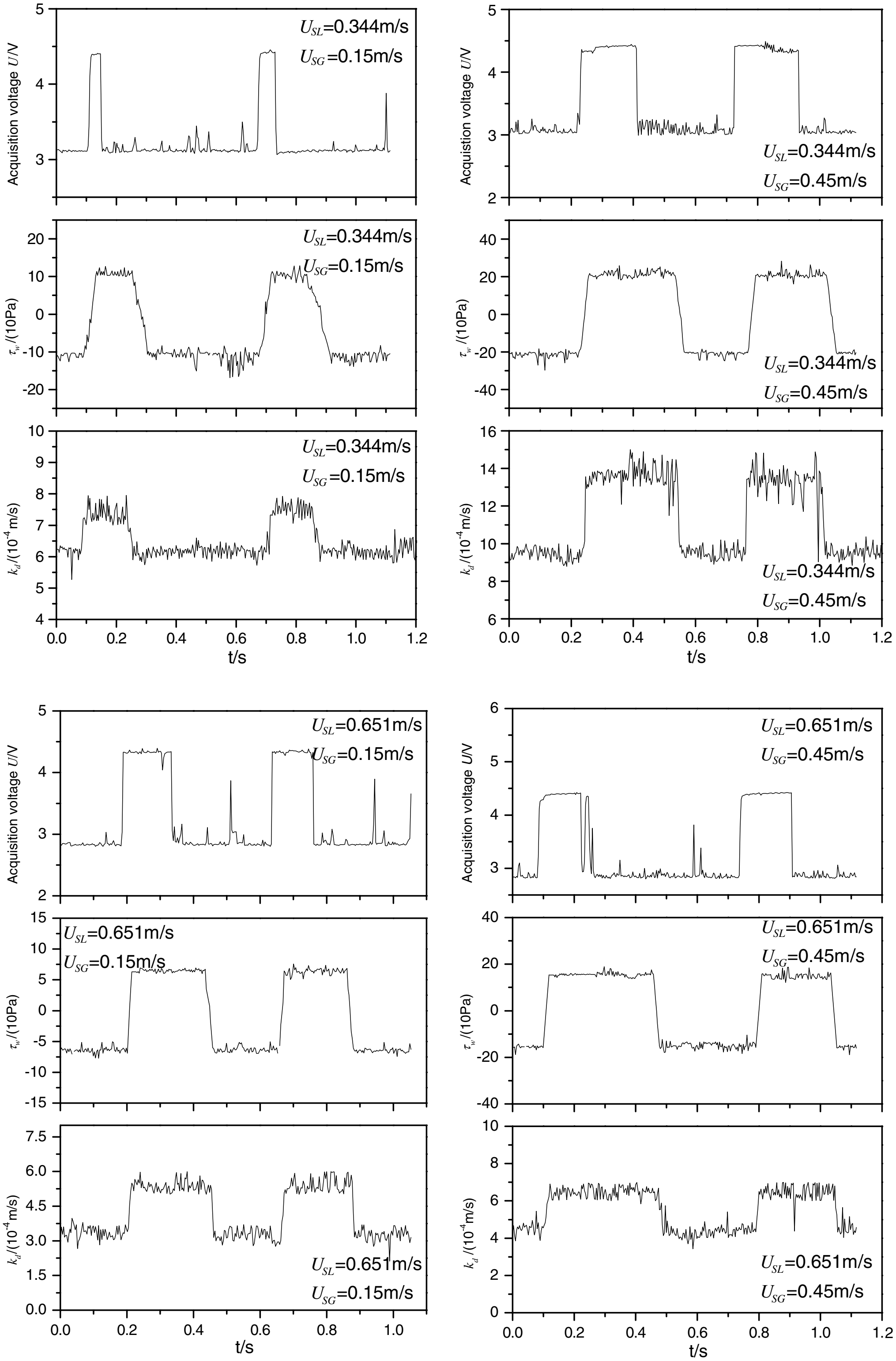

Fig. 24. Wall shear stress and mass transfer coefficient characteristics distribution.

Table 4
The proposed parameter expressions

	k_{df}	k_{dw}	k_{dLS}
U (m/s)	$9.916[gD(1-\langle\alpha_{\mathrm{TB}}\rangle^{0.5})]^{0.5}$	$\langle U_{\mathrm{axial}}\rangle$	$U_{\mathrm{SG}}+U_{\mathrm{SL}}$
L (m)	$4\times 0.5D(1-\langle\alpha_{\mathrm{TB}}\rangle^{0.5})$	D	D
ρ (kg/m^3)	ρ_{L}	$\rho_{\mathrm{L}}(1-\langle\alpha_{\mathrm{LS}}\rangle)+\rho_{\mathrm{G}}\langle\alpha_{\mathrm{LS}}\rangle$	$\rho_{\mathrm{L}}(1-\langle\alpha_{\mathrm{LS}}\rangle)+\rho_{\mathrm{G}}\langle\alpha_{\mathrm{LS}}\rangle$
μ (kg/(m s))	μ_{L}	$\mu_{\mathrm{L}}(1-\langle\alpha_{\mathrm{LS}}\rangle)+\mu_{\mathrm{G}}\langle\alpha_{\mathrm{LS}}\rangle$	$\mu_{\mathrm{L}}(1-\langle\alpha_{\mathrm{LS}}\rangle)+\mu_{\mathrm{G}}\langle\alpha_{\mathrm{LS}}\rangle$

4. Conclusions

Using limiting diffusion current probes, conductivity probes and digital high-speed video system, the characteristics of fully developed gas–liquid two-phase upward slug flow are thoroughly investigated and following conclusions can be drawn:

1. Taylor bubble velocity is not sensitive to the change of liquid viscosity or surface tension, which can be explained by the potential flow theory. The Taylor bubble nose radius of curvature can be represented by $R_0 = 0.71R_c$, and the larger the number Fr_s, the smaller the radius of curvature is. The potential flow theory is inapplicable to the thickness of the falling liquid film far away from the Taylor bubble nose, and the effect of viscosity on the hydrodynamic characteristics should be took into account.
2. The mean thickness and velocity of falling liquid film are in better agreement with the results predicted by Brotz model, whereas the terminal constant thickness δ_t and the terminal constant velocity U_{ft} of falling liquid film are fitted well with Wallis model with $k = 0.103$ and $m = 0.64$ for the turbulent flow at $Re_f > 650$.
3. The penetration length and the Taylor bubble wake length accounts respectively for 10–15% and 18–23% of the liquid slug length, whereas the falling liquid film is formed at the distance of 0.5–1.1D from the Taylor bubble nose in all the experiments. The minimum stable liquid slug length is almost constant and about 7.5–10D. The liquid slug frequency is generally above 2 Hz.
4. The diameters of the dispersed bubbles are within 5.5 mm, and the bubbles with about 1.5–2.5 mm diameter account for 75%. It is also found that the bubbles which appear in the fully developed dispersed liquid slug are within 1.5 mm of diameter and close to be spherical, whereas the bubbles which appear in the wake of Taylor bubble are above 1.5 mm of diameter and more or less distorted. The velocities of dispersed bubbles in liquid slug are found by the experimental results to be fitted well with the model proposed by Zuber and Hench.
5. The length distributions of both the Taylor bubble and the liquid slug are fitted well to the normal distribution. The length of the Taylor bubble, the local void fraction of the slug unit and the liquid slug, the shear stress and the mass transfer coefficient in the near wall zone, are all increased with the increase of superficial gas velocity and decreased with the increase of superficial liquid velocity, whereas both the length and the frequency of liquid slug varies contrarily.
6. Upward gas–liquid slug flow induced corrosion is strongly dependent on the turbulent diffusion mass transfer near the wall. The wall shear stress of upward gas–liquid slug flow in the range of experiments is below 10^3 Pa, which is much less than the adherence of corrosion product film to the metal substrate. Therefore, the alternate wall shear stress is the major cause of the corrosion production film fatigue cracking. The mass transfer coefficient is within 10^{-3} m/s, and a normalized formula for mass transfer coefficient is obtained based on the experimental data.

Acknowledgements

The financial supports from the Natural Science Fund of China (50231020, 10372077) are gratefully acknowledged. The valuable discussions with Prof. Lin HE of Material Science and Engineering School of Xi’an Jiaotong University, Prof. Minxu LU of Material Science and Engineering School of Beijing Science and Technology University, Dr. Zhenquan BAI of Tubular Goods Research Center of China National Petroleum Corporation, and the kind help from them are also gratefully acknowledged.

References

Akagawa, K., Sakaguchi, T., 1966. Fluctuation in void ratio in two-phase flow. Bull. JSME 9, 104–120.

Aladjem Talvy, C., Shemer, L., Barnea, D., 2000. On the interaction between two consecutive elongated bubbles in a vertical pipe. Int. J. Multiphase flow 26, 1905–1923.

Bendiksen, K.H., 1985. On the motion of long bubbles in vertical tubes. Int. J. Multiphase Flow 11, 797–812.

Brotz, W., 1954. Uber die vorausberechnung der absorptionsgeschwindigkeit von gasen in stromenden Flussigkeitsschichten. Chem. Ing. Tech. 26, 470–483.

Brown, R.A.S., 1965. The mechanics of large bubble in tube—I. Bubble velocities in stagnant liquid. Can. J. Chem. Engng. 43, 217–223.

Collier, J.G., Hewitt, G.F., 1964. Film thickness measurements. ASME, paper 64-WA/HT-41.

Collins, R., de Moraes, F.F., 1978. The motion of large gas bubble rising through liquid flowing in a tube. J. Fluid Mech. 89, 497–514.

Davies, R.M., Taylor, G.I., 1950. The mechanics of large bubbles rising through extended liquids and through liquids in tubes. Proc. Royal Soc. A 200, 375–390.

Dukler, A.E., Maron, M.D., Brauner, N., 1985. A physical model for predicting the minimum stable slug length. Chem. Engng. Sci. 40, 1379–1385.

Dumitrescu, D.T., 1943. Stromung an einer Luftblase in senkrechten Rohy. Z. Angew. Math. Mech. 23, 139–149.

Fernandes, R.C., 1981. Experimental and theoretical studies of isothermal upward gas–liquid flows in vertical tubes. Ph.D. thesis, University of Houston.

Fernandes, R.C., Semiat, R., Dukler, A.E., 1983. A hydrodynamic model for gas–liquid slug flow in vertical tubes. AIChE J. 29, 981–989.

Fouad, M.G., IbI, N., 1960. Natural convection mass transfer at vertical electrodes under turbulent flow conditions. Electrochem. Acta 3, 233–243.

Garber, J.D., 1998. Modeling corrosion rates in non-annular gas condensate wells containing CO_2. Corrosion, Houston: NACE, no. 53.

Ghosh, R., Cui, Z.F., 1999. Mass transfer in gas-sparged ultrafiltration: upward slug flow in tubular membranes. J. Membrane Sci. 162, 91–102.

Gognet, G., Lebouche, M., 1978. Utilisation des techniques electrochimiques pour la mesure de frottement parietal dans les ecoulements diphasiques. Houille Blanche 5, 319–322.

Griffith, P., 1963. The slug-annular flow regime transition at elevated pressure. Argonne Rep. ANL-6796.

Griffith, P., Wallis, G.B., 1961. Two-phase slug flow. Trans. ASME J. Heat Transfer 83, 307–320.

Hanratty, T.J., Reiss, L.P., 1962. Measurement of instantaneous rate of mass transfer to a small sink on a wall. AIChE J. 8, 245–250.

Hara, T., Asahi, H., Suehiro, Y., et al., 2000. Effect of flow velocity on carbon dioxide corrosion behavior in oil and gas environments. Corrosion 56, 860–866.

Harmathy, T.Z., 1960. Velocity of large drops and bubbles in media of infinite of restricted extent. AIChE J. 6, 281–288.

Heitz, E., 1991. Chemo-mechanical effects of flow on corrosion. Corrosion 47, 135–145.

Heuer, J.K., Stubbins, J.F., 1998. Microstructure analysis of coupons exposed to carbon dioxide corrosion in multiphase flow. Corrosion 54, 566–575.

Hewitt, G.F., 1990. Multiphase fluid flow and pressure drop: introduction and fundamentals. In: Hewitt, G.F. (Ed.), Hemisphere Handbook of Heat Exchanger Design. Hemisphere, New York.

Hewitt, G.F., Lovegrove, P.C., 1963. Film thickness and holdup measurements, AERE-M-1203, United Kingdom Atomic Energy Authority.

Jasinski, R., 1987. Corrosion of N80-type steel by CO_2–water mixtures. Corrosion 43, 214–218.

Juprasert, S., 1976. Two-phase flow in an inclined pipeline-riser pipe system. M.S. thesis, University of Tulsa.

Kordyban, E.S., Ranov, T., 1963. Experimental study of the mechanism of two-phase slug flow in a horizontal tube. Winter Annu. ASME Symp. on Multiphase flow, Philadelphia, paper no. 053.

Liu, T.J., Bankoff, S.G., 1993. Structure of air–water bubbly flow in a vertical pipe—I. Liquid mean velocity and turbulence measurements. Int. J. Heat Mass Transfer 36, 1049–1060.

Liu, G., Tree, D.A., High, M.S., 1994. Relationship between rotating disk corrosion measurements and corrosion in pipe flow. Corrosion 50, 584–593.

Lotz, U., Syberger, T., 1988. CO_2 corrosion of carbon steel and 13Cr steel in particle-laden fluid. Corrosion 44, 800–809.

Mao, Z.S., Dukler, A.E., 1985. Rise velocity of a Taylor bubble in a train of such bubbles in a flowing liquid. Chem. Eng. Sci. 40, 2158–2160.

Moissis, R., Griffith, P., 1962. Entrance effects in two-phase slug flow. J. Heat Transfer 84, 29–39.

Mora-Mendoza, J.L., Chacon-Nava, J.G., et al., 2002. Influence of turbulent flow on the localized corrosion process of mild steel with inhibited aqueous carbon dioxide systems. Corrosion 58, 608–618.

Nakoryakov, V.E., Kashinsky, O.N., 1981. Local characteristics of upward gas–liquid flow. Int. J. Multiphase flow 7, 63–81.

Nakoryakov, V.E., Kashinsky, O.N., Kozmenko, B.K., 1986. Experimental study of gas–liquid slug flow in a small-diameter vertical tube. Int. J. Multiphase flow 12, 337–355.

Nesic, S., Lunde, L., 1994. Carbon dioxide corrosion of carbon steel in two-phase flow. Corrosion 50, 717–883.

Nesic, S., Solvi, G.T., Enerhaug, J., 1995. Comparison of the rotating cylinder and pipe flow test for flow-sensitive carbon dioxide corrosion. Corrosion 51, 773–787.

Nicklin, D.J., Wilkes, J.O., 1962. Two-phase flow in vertical tubes. Trans. Inst. Chem. Eng. 40, 61–68.

Ozgu, M.R., Chen, J.C., Stenning, A.H., 1973. Local liquid film thickness around Taylor bubbles. ASME J. Heat transfer 95, 425–427.

Reiss, L.P., Hanratty, T.J., 1963. An experimental study of the unsteady nature of the viscous sublayer. AIChE J. 9, 154–160.

Schmidt, Z., 1976. Experimental study of gas–liquid flow in a pipeline-riser pipe system. M.S. thesis, University of Tulsa.

Schmitt, G., Bosch, C., Mueller, M., 1999. Modeling the probability of flow induced localized corrosion from critical hydrodynamic data and fracture mechanics data of scales from CO_2 corrosion of steel. In: Advances in Corrosion Control and Materials in Oil and Gas Production. European Federation of corrosion, The Institute of Materials, London.

Shemer, L., Barnea, D., 1987. Visualization of the instantaneous velocity profiles in gas–liquid slug flow. PhysicoChem. Hydrodynam. 8, 243–253.

Solomon, V.J., 1962. Construction of a two-phase flow regime transition detector. M.S. thesis. Mechanical Engineering Department, MIT.

Souhar, M., Cognet, G., 1978. Electrochemical method for dynamic measurements in two-phase flow. In: Proceedings of the Dynamic Flow Conference, Marseille, pp. 363–369.

Street, J.R., Tek, M.R., 1965. Dynamics of bullet shaped bubbles encountered in vertical gas liquid slug flow. AIChE J. 11, 644–650.

Sylvester, N.D., 1987. A mechanistic model for two-phase vertical slug flow in pipes. ASME J. Energy Resources Technol. 109, 206–213.

Taitel, Y., Barnea, D., Dukler, A.E., 1980. Modeling flow pattern transitions for steady upward gas–liquid flow in vertical tubes. AIChE J. 26, 345–354.

van Hout, R., Barnea, D., Shemer, L., 2001. Evolution of statistical parameters of gas–liquid slug flow along vertical pipes. Int. J. Multiphase flow 27, 1579–1602.

Wallis, G.B., 1969. One-dimensional Two-phase Flow. McGraw-Hill, New York.

Zuber, N., Hench, J., 1962. Steady state and transient void fraction of bubbling systems and their operating limit. Part I: Steady state operation. General Electric Report, 62GL100.